The GFDL CM4X Climate Model Project

Development of CM4_C192_OM4p25 and CM4_C192_OM4p125

June 11, 2026

Stephen.Griffies@noaa.gov and GFDL Oceans + Cryosphere Division (O-division)

In May 2020, two months into the COVID-19 shutdown, the GFDL O-Division embarked on the CM4X project to further an ability to numerically model physical processes in support of GFDL and NOAA's research missions. The upper member of the hierarchy, CM4_C192_OM4p125, has double the ocean and atmosphere resolution relative to the CMIP6 version of CM4.0 (*Held et al.*, 2019). This doubling of the resolution motivates the name CM4X for the project. This report documents development of the CM4X hierarchy of models. It provides unpublished notes that supplement the two published JAMES papers *Griffies et al.* (2025a,b)

The CM4X project aims to develop a suite of GFDL coupled climate models supporting research into the role of the ocean in the earth climate system, with particular attention given to the role of ocean mesoscale features as well as boundary currents. For the atmosphere and land model components of CM4X, we make use of the C192 (nominally 50 km horizontal grid spacing) version of GFDL/AM4 as documented in *Zhao* (2020), whereas the CM4.0 model of *Held et al.* (2019) used the nominal C96 grid (nominally 100 km grid spacing). The C192 atmospheric grid supports stronger tropical and mid-latitude cyclones than the C96 grid, with such cyclones key features of planned research on ocean extremes using the CM4X models. For the ocean (MOM6) and sea ice (SIS2), we develop a hierarchy of horizontal grids with nominal spacing of 0.25° and 0.125°. The ocean and sea ice configurations are based on those from OM4.0 as documented by *Adcroft et al.* (2019), yet with important updates to numerical methods and physical parameterizations as identified in this report.

Contents

1 Loose threads

- Document the issue with the displaced pole and the problems with xh. Show some grid lines.

2 The CM4X Project

The ocean is the predominant reservoir in the earth climate system for enthalpy (heat) and carbon, and the ocean circulation redistributes these properties throughout the World Ocean. A zoo of physical processes spanning a wide space-time range of scales contribute to how the ocean works as part of the earth climate system, with Figure 1 providing a cartoon for some of these processes. The GFDL Oceans/Cryosphere Division conducts scientific research aimed at understanding these and related physical processes; considers how to represent/parameterize processes in climate models; and examines how these processes play a role in the earth's climate, including its long term mean, temporal variability, and human induced changes. The CM4X project aims to provide a tool that expands the division's ability to address its core mission.

2.1 Key ocean and ice processes of interest

The CM4X project is motivated in part by the O-division's quest to further scientific understanding of how ocean mesoscale features affect the large-scale ocean general circulation as well as the earth's climate. It is also motivated by the need to better represent boundary and shelf processes that play a critical role in both the large-scale circulation and form the ocean region of highest impact on humans, namely the coastal region. These goals encompass a huge suite of phenomena: basin-wide current systems (gyres, overturning circulation, equatorial currents) that form the large-scale mean circulation patterns; transient mesoscale eddies (the ocean's "weather") that dominate the ocean's kinetic energy; boundary currents and boundary waves that affect shelf and nearshore processes; submesoscale fronts and eddies that interact with mesoscale eddies and boundary currents; gravity waves that feed off the vertical stratification; vertical convection arising from gravitationally unstable fluid columns with heavy water above lighter water; and small-scale three dimensional turbulence in the ocean interior (arising from breaking internal gravity waves) and next to boundaries (arising from shear instability, Langmuir turbulence, and other boundary processes). The cryosphere also plays a huge role in earth's climate, with mesoscale features interacting with the cryosphere in the polar regions where ice-shelves and sea-ice influence the climate by modifying albedo (reflectivity) as well as altering how fluxes are exchanged between the ocean and atmosphere. Furthermore, interactions between the ocean and ice-shelves, icebergs, and sea-ice influence the rate of ice melt, sea-level rise and large-scale ocean currents.

2.2 Grid spacing considerations

A faithful numerical depiction of the ocean and cryosphere, and its interactions with the atmosphere and land, requires coupled climate models with relatively fine grid spacing, in both the horizontal and vertical, as well as a realistic suite of physical, chemical, and biological processes. Our focus concerns the physical aspects of the ocean and sea ice model components. We thus take the atmosphere and land models largely unchanged from the C192 (nominally 50 km grid spacing) version of AM4 as documented by *Zhao* (2020). We use C192 horizontal grid for CM4X to support a better representation of tropical

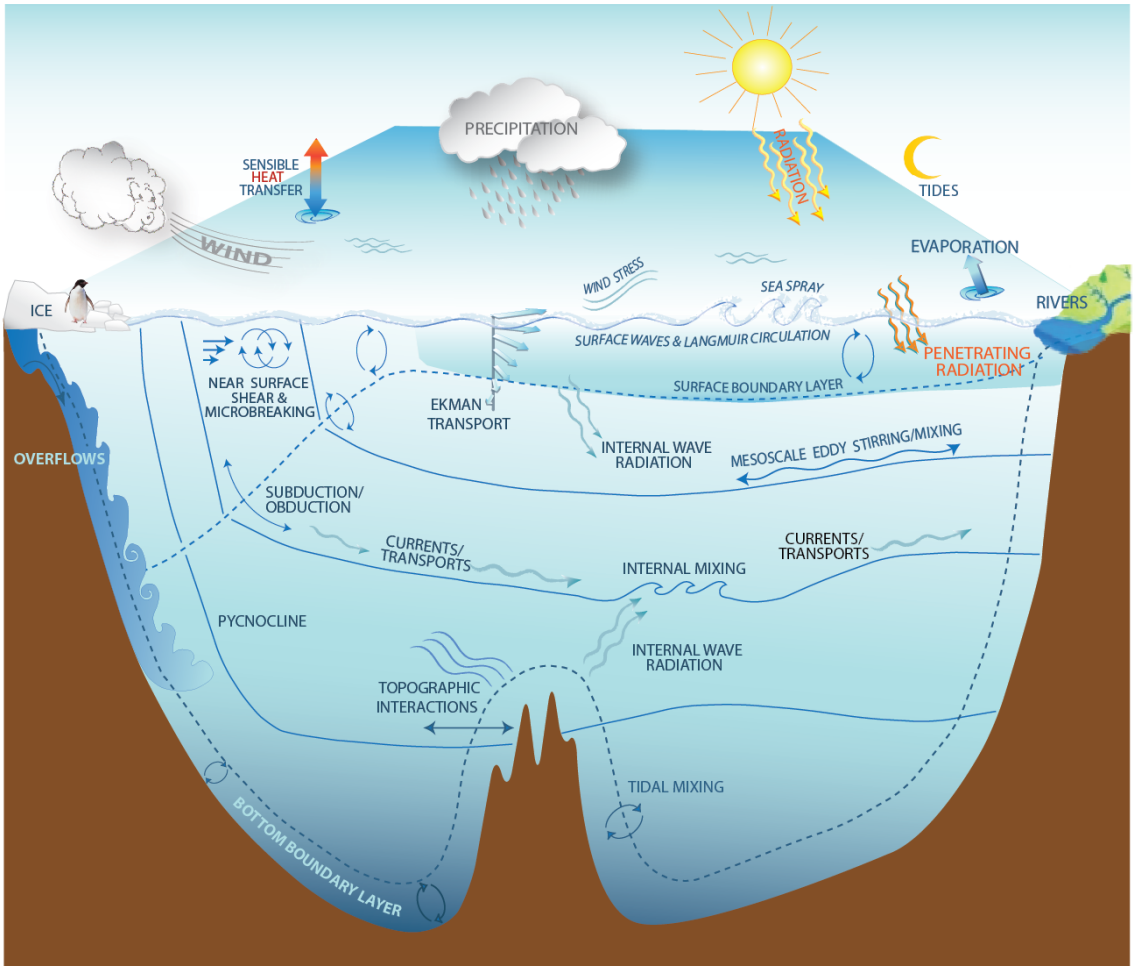

Figure 1: A schematic of the zoo of ocean processes contributing to how the ocean works as part of the climate system. This figure is taken from *Griffies and Treguier* (2013).

and middle latitude cyclones than available from the C96 atmospheric grid as used for CM4.0 (*Held et al.*, 2019). Such atmospheric cyclones have an important imprint on ocean extreme events related to sea level and ocean heat waves, which are two key research areas targeted for the CM4X project.

We acknowledge that a grid refinement by a factor of two is insufficient to resolve many of the key physical processes important especially for high latitude climate. *Hallberg* (2013) and *Griffies and Treguier* (2013) argued that a useful metric for grid spacing is based on the first baroclinic Rossby radius, with this scale relevant for ocean mesoscale features and boundary currents/waves. As shown by Figure 2, taken from *Hallberg* (2013), a 0.125° grid spacing is insufficient to resolve the first baroclinic Rossby radius in the high latitudes as well as on the continental shelves.

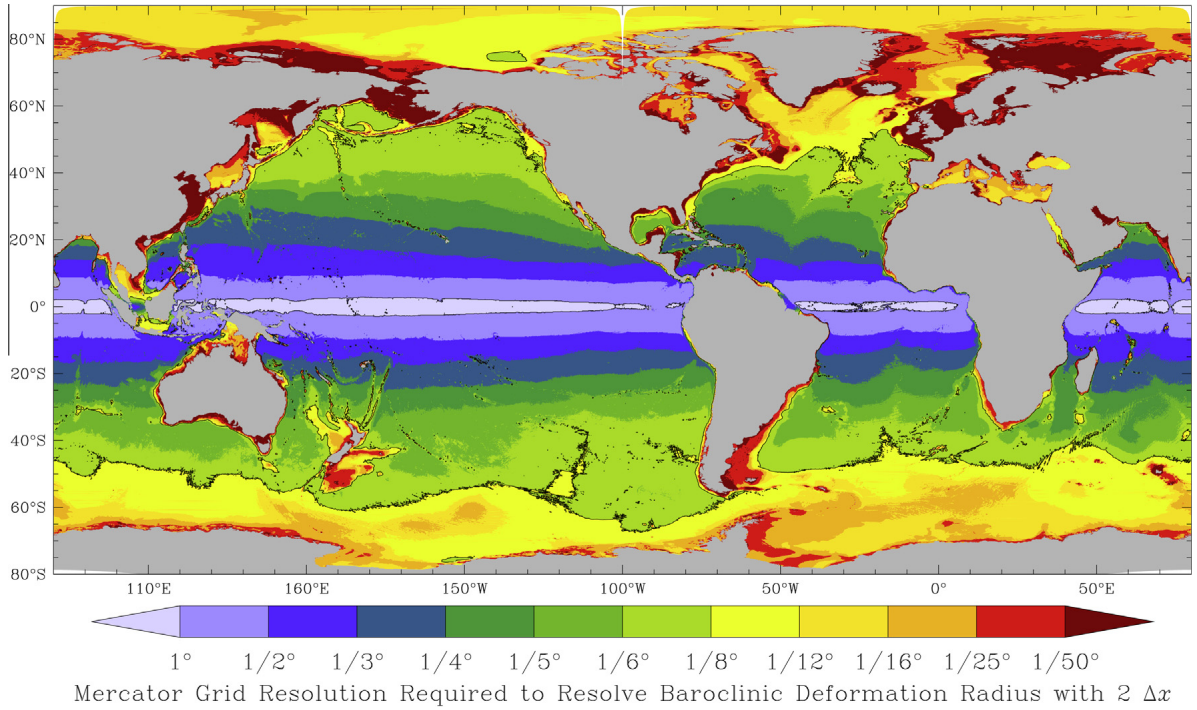

Figure 2: The horizontal grid spacing needed to resolve the first baroclinic deformation radius with two grid points, based on a 0.125° GOLD simulation on a Mercator grid on Jan. 1 after one year of spinup from climatology. The solid line shows the contour where the deformation radius is resolved with two grid points at 1° and 0.125° grid spacings. This figure is taken from *Hallberg* (2013).

2.3 Science aspirations balanced by computer resources

GFDL has a successful history developing climate models that make use of grid resolution hierarchies, with the CM2-O climate model suite a recent example (*Griffies et al.*, 2015). There is great practical value in a step-wise approach to model development, whereby diagnostic tools and experience garnered from previous efforts, such as OM4.0 and CM4.0, offer essential foundations for new development. Quite simply, we learn much about modeling science and engineering in the process of incrementally refining grid spacing.

We chose the 0.125° for CM4X partly in recognition of computer resources available to the O-Division. We plan to use this model for centennial-scale simulations such as the CMIP-Deck, along with allied perturbation and sensitivity experiments. Hence, we chose not to push the grid spacing too fine as doing so would compromise our ability to run multiple centennial simulations, both for production and development. Even so, the 0.125° grid allows for a realistic representation of flow regimes as well as the interaction of these flows with the complex land/sea geography. Furthermore, it provides a marginally sufficient grid spacing to meaningfully couple with a dynamic ice shelf model, with this coupling a target for development once the baseline climate model is configured. Finally, it provides a firm foundation for development of even finer grid models when computer resources become available.

2.4 Some philosophical points

In developing new models, it is crucial to maintain a balance between what is practical and what is aspirational. In particular, we have learned to be respectful of **Hofstadter's Law** (*Hofstadter*, 1979), here paraphrased for climate model development:

> **Hofstadter's Law** (paraphrased): Climate model development always takes longer than you expect, even when you take into account Hofstadter's Law.

This law is partnered with the following:

> **Hallberg's Principle**: Numerical models closely approximate Murphy's Law Machines: anything that can go wrong will go wrong and will go wrong when least desired.

It is furthermore supported by

> **Stouffer's Principle**: Numerical model development is a process, not an event.

Accepting the wisdom of the above, we are led to the following:

> **Model Developer's Practice of Humility**: Acceptance of Hofstadter's Law, Hallberg's Principle, and Stouffer's Principle, promotes the wisdom of a humble, documented, stepwise model development process that rests on the shoulders of previous model generations while cautiously probing new frontiers.

Quite simply, an arrogant approach to model development is always penalized. We are motivated to write this report as a means to help document and rationalize the CM4X development process, and to offer our experience to future generations of model developers.

2.5 Model hierarchies

Scientific descriptions of Nature commonly use hierarchies of theoretical models. The theoretical models used for earth system science are mathematical in nature and must generally be realized numerically since the equations are highly nonlinear and are applied over complex spatial geometries. Numerical models are a ubiquitous feature of earth system science, thus providing repositories for theories of how the earth system works from a process perspective. By allowing processes to interact across space-time scales, numerical models offer an experimental tool to explore mechanisms for emergent phenomena such as the ocean and atmosphere general circulation and coupled fluctuations involving multiple components of the earth climate system. An extension of this approach pursues an increasingly large number of processes that support the probing of earth system phenomena while offering predictive skills important for applications such as weather forecasts, climate prediction, and the development of resilient societies.

Realism and completeness often run counter to the needs for unpacking the underlying physical mechanisms rendering scientific insights and robust understanding. This situation motivates the development of idealized process models that better control for the processes under investigation. As emphasized by (*Held*, 2005) and *Jeevanjee et al.* (2017),

model hierarchies provide a crucial bridge that spans the spectrum between realistic and idealistic. Such hierarchies support the science forming the basis of earth system models, and enhance the science emerging from their simulations.

A model hierarchy is often realized by a suite of distinct equations that span across a spectrum of theoretical complexity. One example is the hierarchy of mathematical models used to study geostrophic turbulence, with barotropic two-dimensional f-plane turbulence at one end of the spectrum, whereas continuously stratified quasi-geostrophic beta-plane turbulence sits at the more complex end. For CM4X, we are instead concerned with a model hierarchy that utilizes the same mathematical equations, namely the hydrostatic ocean primitive equations posed on a realistic global domain.

The CM4X hierarchy is realized by examining simulations from a suite of grid resolutions that realize distinct flow regimes. So in this manner, we are considering a hierarchy of model configurations where the grid spacing is the only difference between members of the hierarchy. As the grid spacing is refined, the role of the nonlinear transport terms in the fluid equations (i.e., advection) becomes more prominent, which generally results in stronger flows that exhibit transient and/or turbulent behavior. A grid resolution hierarchy is concerned with questions of convergence, both numerically and physically. More practically, we seek specific examples for what advantage we realize by refining ocean grid spacing. Answers to this question affect how we allocate resources across the O-division and GFDL.

Among the various hierarchies considered by (*Jeevanjee et al.*, 2017), they included grid resolution hierarchies for the purpose of studying atmospheric convection using the same model equation set realized with different grid spacing. We follow the same approach here for the CM4X hierarchy. However, our focus concerns the ocean mesoscale as well as ocean boundary currents, with interest in both the dynamics of these features and their role in the earth climate system. The GFDL CM2-O model suite (*Griffies et al.*, 2015) is an earlier example of a model hierarchy with similar goals. In the CM2-O suite, three ocean models of varying grid spacing are coupled to the same land and atmosphere models. The CM2-O model suite forms the basis for roughly 45 peer-reviewed papers, which exemplifies the rather rich suite of science questions that can be addressed with carefully constructed grid spacing hierarchies. Further examples of ocean grid hierarchies include *Kiss et al.* (2020), with their ocean-sea ice hierarchy built using MOM5 and taking the CM2-O hierarchy as a starting point, and *Marques et al.* (2022), which targets ocean mesoscale eddy features using an adiabatic stacked shallow water version of MOM6. See *Jeevanjee et al.* (2017) for a listing of the many hierarchy papers focused on atmospheric processes.

2.6 Specific applications for the CM4X project

We learned a tremendous amount about modeling the earth climate system in the process of developing CM4.0 (*Held et al.*, 2019) and in its ongoing analysis. This model, and its ocean/sea ice component OM4.0 (*Adcroft et al.*, 2019), are among the world's best models of the earth climate system. Even so, we aim here to do better both by refining grid spacing and by improving subgrid scale parameterizations. Doing so will expand the suite of research problems that can be considered. The following offers a sample list of questions that we plan to address with this model hierarchy (as of 2022).

- Heat uptake + global thermosteric sea level + regional sea level (especially continental shelves)
  - Mesoscale eddy effects on heat uptake in transient simulations (analog to CM2.5 vs CM2.6 as detailed by *Griffies et al.* (2015)).
  - Relevant to the broader O-division science.
- Ocean extremes (especially on continental shelves) with the C192 atmospheric storms of particular importance, with applications to sea level and ocean heat waves.
  - NOAA east coast sea level grant with L. Zanna, J. Yin, Griffies + NYU postdoc
  - NOAA CMIP project on sea level with Krasting, Griffies, and Tesdal (in collaboration with Rutgers and Billy Sweet)
  - NOAA east coast sea level project with C. Little, Krasting
  - Marine heat waves project sponsored by the Model Diagnostics Task Force: Krasting + postdoc.
- Southern Ocean dynamics, including a resolved Antarctic Slope Current:
  - Processes related to ventilation pathways and overflows
  - Watermass transformations
  - Beadling, MacGilchrist, Tesdal, Krasting, Griffies + SOCCOM
  - DOE project with Griffies, Krasting and postdoc funds for MacGilchrist and Tesdal.
- AMOC mean, variability, and stability + connections to Arctic
  - R. Zhang, Thomas
  - Bushuk, Winton, Y. Zhang
- Ice shelf coupling
  - topography built from GEBCO+Bedmachine to capture ice shelf cavities.
  - Sergienko, Hallberg, Harrison, Adcroft, Dussin, postdocs
- Topographic interactions; boundary currents; momentum and vorticity dynamics
  - Refined resolution yields more dynamical ocean to support GFD-style analysis.
  - MacGilchrist, Sonnewald, Khatri (Liverpool), Griffies
- High latitude overflows
  - Legg
- Mesoscale eddy parameterization CPT

  - Provide global model data with highly energetic eddy field for use in studies of eddy dynamics.
  - Adcroft, Hallberg, Griffies and postdocs Chang + W. Zhang

- Tropical climate, surface waves, cyclones, and ocean mixing
  - Reichl, Legg, collaborators

- Biogeochemistry: ongoing discussions with B-division

In building the hierarchy, we must maintain a view on the climate relevant metrics that allow us to declare the development effort to be successful or not. The following lists a few of the key metrics that concern members of the O-Division, where we hope to do better, or at least no worse, than CM4.0:

- mixed layers, SST, SSS, SSH
- stable and deep AMOC and OSNAP flows
- strong AABW and Drake Passage transport with realistic (not super strong) polynyas
- ocean heat uptake
- large scale patterns such as ENSO, SAM, PDO
- boundary currents: Gulf Stream, Kuroshio, East Australia, Antarctic Slope

Finally, here are a few model capabilities that are desirable:

- sea ice displacing water to allow grounded ice + shelves (requires new coupling from RWH)
- No crashes and no "bit switch" tricks

2.7 Tuning SST and heat uptake: importance of vertical transport

For the middle latitude gyres, CM4.0 generally has a cool SST bias and warm sub-surface bias along with too much volume mean ocean heat uptake. This cool over warm bias is largely a signature of ocean vertical transport, though atmospheric radiative balance plays a role in the overall heat uptake. From the ocean side, if we realize a stronger vertically upward buoyancy transfer from mesoscale eddies, as expected from the p125 degree ocean relative to the p25 ocean, then the cold over warm bias should reduce. This expectation is based on the comparison of CM2.6 (p10 grid) versus CM2.5 (p25 grid) (*Griffies et al.*, 2015).

Alternatively, we can realize more vertically upward transport of buoyancy via the submesoscale parameterization (MLE scheme). Indeed, for CM4.0, there is no mesoscale eddy closure, so the MLE scheme is the main ocean tuning knob for upward vertical buoyancy transfer. Unfortunately, the CM4.0 settings for the MLE scheme are unphysical in that it is acting far too strongly relative to process studies. That is, the MLE scheme in

CM4.0 provides unphysically large restratification by dialing up the strength and duration of the MLE overturning streamfunction. For the CM40-2X configuration, we are hoping to reduce, at least to some degree, the affects from the MLE scheme (see Section 15) while still maintaining a viable climate model. Furthermore, we expect to be able to tune down the MLE scheme when running with the p125 ocean since this grid realizes stronger mesoscale eddy transport than the p25 grid. Even so, we might not be able to turn MLE down as much as desired, with that conclusion depending on the atmosphere radiative balance.

3 Centenniel scale piControl experiments

During development, we focus on pre-industrial control experiments that use radiative forcing fixed at 1850 levels. These experiments were initially run for a few decades in length, which was long enough to identify problems. Thereafter, we ran for 100+ years to better determine the integrity of a decadal-centennial scale climate mean and variations. The following summarizes those p125 simulations of 100+ years duration, which is long enough to identify possible problems with ENSO, AMOC, ACC, sea ice, ocean heat uptake, etc.

- Odiv-155 (100 years): this was the first long run.
- Odiv-169 (150 years): This experiment had an issue with the land model and river network.
- Odiv 183/184 (200 years): Ran with bad vertical remapping scheme, thus causing extensive loss of interior stratification (see Section 8).
- Odiv-200 (200 years): Many positive features, but decided that the sea ice albedos and land ice albedos needed to be modified to return to CM4.0 and ESM4.0 values, respectively. The key features that were found deficient concerned the Southern Ocean ventilation (virtually no AABW), ACC strength (too weak and ongoing decline of thermal wind component), and Antarctic Slope Current strength (too strong).
- Odiv-209: running now with ESM4 land ice albedo and CM4.0 sea ice albedo. Both are aimed to enhance the ventilation in the Southern Ocean and increase sea ice thickness particularly in the summer.

4 Horizontal grid

The horizontal grid generation repository is

```
https://github.com/nikizadehgfdl/ocean_model_grid_generator
```

We make use of a locally orthogonal coordinate grid with a nominal resolution of 0.125 degrees along the equator. The grid consists of a Mercator layout spanning

$$\text{Mercator} \in [-66.8840965847^{\circ}, 64.0316059408^{\circ}], \tag{1}$$

MODEL	GRID SPACING	GRID RESOLUTION
OM4p25	nominal 0.25°	1440×1080
OM4p125	nominal 0.25°	2880×2240

Table 1: Summary of the horizontal grid spacing and horizontal grid resolution for the CM4 model suite. The term "nominal" reflects the non-uniform nature of the grid according to the Mercator projection and bipolar Arctic (see Figure 3). All configurations share the same 75-layer hybrid vertical grid realized using the vertical Lagrangian remap method (*Adcroft et al.*, 2019; *Griffies et al.*, 2020).

flanked by a bipolar northern cap and a regular latitude/longitude grid spanning

$$\text{regular lat-lon} \in [-78^\circ, -66.8840965847^\circ]. \tag{2}$$

It is capped by a displaced pole grid south of -78.0°, with the southern displaced pole motivated by ice-shelf studies (Figure 3). The first five southern rows are deleted.[1] The number of grid points is

$$N_x \times N_y = 1440 \times 1080 \quad \text{p25 grid} \tag{3a}$$
$$N_x \times N_y = 2880 \times 2240 \quad \text{p125 grid} \tag{3b}$$

Table 1 summarizes the horizontal grid specifications, and more on the horizontal grid can be found in Section 2.1.2 of *Adcroft et al.* (2019). Note that for precision in language, we use the term *resolution* for the number of degrees of freedom, with resolution a pure number. As a complement, *grid spacing* refers to the distance between grid cells and is measured in degrees or kilometers.

Figure 4 shows the regional basin mask used to facilitate regional diagnostics. This mask was generated using code in the following repository:

```
https://github.com/jkrasting/cmip_basins
```

5 Bottom topography

For the 0.25° configuration, we retained the same bottom topography as used for the OM4.0 model documented by *Adcroft et al.* (2019). Unfortunately, much of that development was not fully documented. We here document the steps used to develop the p125 topography, with particular attention given to the southern high latitude regions due to the planned use of this model for ice-shelf studies. For both models we have the minimum and maximum depths set according to

$$\texttt{MINIMUM\_DEPTH} = 9.5 \text{ m} \tag{4a}$$
$$\texttt{MAXIMUM\_DEPTH} = 6500 \text{ m}. \tag{4b}$$

[1] I forget why???

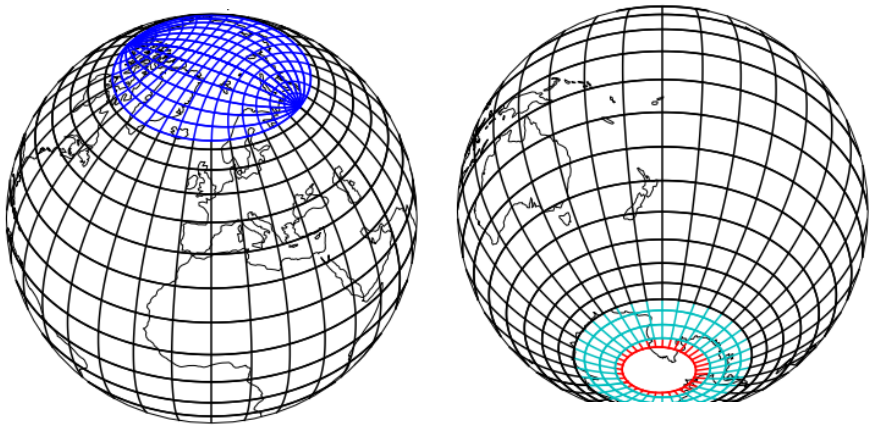

Figure 3: Horizontal grid for the OM4.0 model, with the same layout used for the CM4X ocean model components. Only every 20th grid line is plotted. Black/blue/cyan/red lines indicate the Mercator grid, bipolar Arctic cap, spherical grid, and twisted south pole grid. This image was adapted from Figure 1 of *Adcroft et al.* (2019).

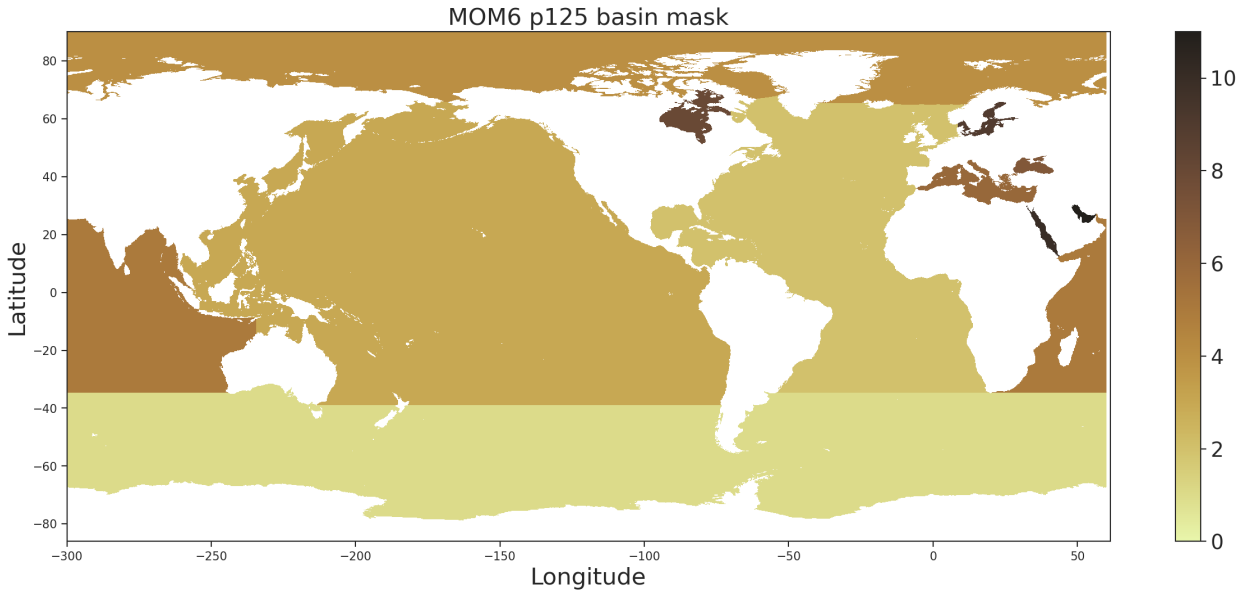

Figure 4: Ocean basin mask for use in diagnostic calculations. There are 11 distinct basins with values: 1=Southern Ocean, 2=Atlantic Ocean, 3=Pacific Ocean, 4=Arctic Ocean, 5=Indian Ocean, 6=Mediterranean Sea, 7=Black Sea, 8=Hudson Bay, 9=Baltic Sea, 10=Red Sea, 11=Persian Gulf.

5.1 GEBCO2 and BedMachine

The bottom topography for the p125 ocean is based on *GEBCO Compilation Group* (2021). This topography provides global coverage on a 15 arc-second interval grid. We downloaded this data from

```
https://www.gebco.net/data_and_products/gridded_bathymetry_data/
```

GEBCO provides under-ice topography for Greenland and a modest level for Antarctica.[2] For the region south of 62°S we transitioned to the BedMachine product from *Morlighem et al.* (2017) since BedMachine offers much more information about the Southern Ocean and goes further inland to capture ice-shelf cavities. We did not use BedMachine for Greenland since we assume that GEBCO makes use of sufficient data coverage for Greenland to satisfy our uses, and because our initial applications for ice-shelves have Antarctica as the focus.

5.2 Technical details

Here are the technical details for the topography generation, with pointers to the various repositories for software.

5.2.1 Regridding BedMachine to GEBCO

We placed the BedMachine data onto the GEBCO grid using linear remapping as realized in the following repositories:

```
https://gitlab.gfdl.noaa.gov/ogrp/regrid_weights_bedmachine_gebco
https://github.com/raphaeldussin/OM4_125_bedmachine_ant1/tree/master/raw_data
```

Notebooks for the regrid step and then a merger of the GEBCO and BecMachine topography are found in this repository:

```
https://gitlab.gfdl.noaa.gov/ogrp/cm4_omp125_c192_bathy
```

and the merged topography is in this NetCDF file

```
/net2/rnd/OM4_125_bedmachine_ant1/raw_data/merged_BedMachineAntarctic_GEBCO2.nc
```

5.2.2 Mapping topography to model grid

After the merged topography was generated, we interpolated this topography to the p125 ocean model grid using code in this repository

```
https://github.com/nikizadehgfdl/ocean_model_topog_generator
```

This tool creates a model topography for a given horizontal model grid and a given observation dataset for height. It uses a recursive refine-sample-coarsen scheme to interpolate

[2] SRTM15 from *Tozer et al.* (2019) does not provide under-ice topography, which prompted us to use GEBCO.

the observation dataset onto the model grid. This tool is based on the algorithm of *Adcroft* (2013) for interpolating topography, with software hosted in this repository:

```
https://github.com/adcroft/thin-wall-topography
```

5.2.3 Partial openings for restricted straights

On a coarsened grid there are straights that are artificially closed due to limitations of grid spacing. However, certain openings are particularly important for water masses of the World Ocean. A primary example is the Straight of Gibraltar that connects the Atlantic and Mediterranean, with this straight roughly 10 km across. Conversely, there might be straights that are opened on a grid that are unwarranted, and so need to be closed.[3] These considerations make it necessary to hand-tune special passages and straights to enable flow if artificially closed (e.g. Gibraltar), or to close straights that are best kept closed (e.g., Lake Maracaibo in Venezuela). This tuning is handled by scanning topography mapped to the ocean model grid and comparing to an atlas (e.g., National Geographic). One then steps through the World Ocean region-by-region to examine the integrity of the topography. The details of this work are documented in the Python script

```
https://gitlab.gfdl.noaa.gov/ogrp/cm4_omp125_c192_bathy/OM4p125_edit_topo.ipynb
```

The hand-tuning works on a cell-by-cell basis, opening or closing straights according to the size of the grid cell. MOM6 provides the added feature of being able to restrict the openings of channels to a width corresponding to observed values. For the p125 grid we provide information about the restrictions in the runtime file

```
MOM_channels_global_125
```

Restrictions are given in this file for the following three straights: Dardanelles, Bosporus, and between Sakhalin & Russia.

5.3 Ice9 algorithm

After the hand-tuning process is complete, we apply the following Python implementation of the ice9 algorithm to ensure there are no land-locked ocean regions:

[3] For the C-grid of MOM6, flow through openings is available with a single grid tracer cell, whereas the B-grid of earlier MOM codes requires two tracer cells. Hence, the C-grid allows for a more detailed representation of the complex geography of the World Ocean than the B-grid.

```
def ice9it(i,j,depth):
  # Iterative implementation of "ice 9"
  wetMask = 0*depth
  (nj,ni) = wetMask.shape
  stack = set()
  stack.add( (j,i) )
  while stack:
    (j,i) = stack.pop()
    if wetMask[j,i] or depth[j,i] >= 0: continue
    wetMask[j,i] = 1
    if i>0: stack.add( (j,i-1) )
    else: stack.add( (j,ni-1) )
    if i<ni-1: stack.add( (j,i+1) )
    else: stack.add( (0,j) )
    if j>0: stack.add( (j-1,i) )
    if j<nj-1: stack.add( (j+1,i) )
    else: stack.add( (j,ni-1-i) )
  return wetMask
```

5.4 Resulting topography

Figure 5 depicts the topography resulting from the above multi-step algorithm, along with GEBCO masking applied to the BedMachine ice-shelf regions around Antarctica since we are not yet running this model with ice-shelves. This data is located at

```
/archive/Raphael.Dussin/datasets/OM4p125/
mosaic_c192_om4p125_bedmachine_v20210310_hydrographyKDunne20210614_unpacked/
ocean_topog.nc
```

6 Vertical grid

For the vertical grid, we follow the hybrid vertical coordinate discussed in Section 2.1.4 of *Adcroft et al.* (2019), motivated by the "HYCOM" approach of *Bleck* (2002). In this approach, CM4X makes use of a hybrid vertical coordinate in which the upper ocean interfaces are aligned with z^* quasi-geopotential surfaces, whereas the interior surfaces are aligned with potential density referenced to 2000 dbar. This vertical grid is realized by setting

$$\texttt{REGRIDDING\_COORDINATE\_MODE} = \texttt{"HYCOM1"} \tag{5}$$

in the parameter file. There are 75 layers in total for any particular column, though some of those layers can have zero thickness depending on the density.

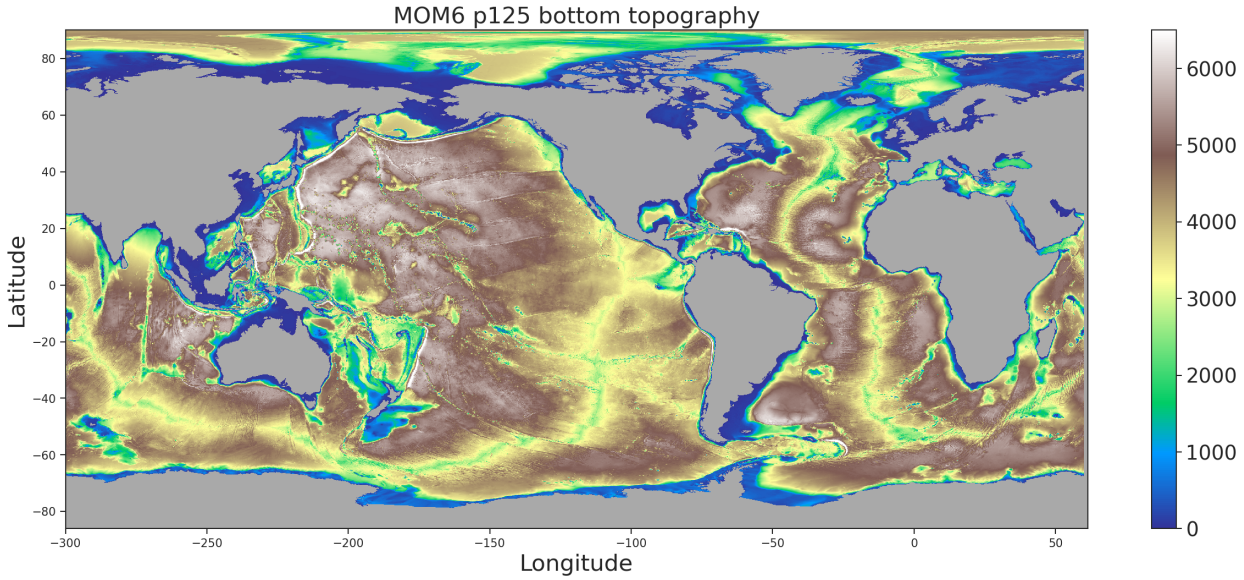

Figure 5: Ocean bottom topography for p125 MOM6 model configuration.

The bottom topography is represented using a linear piecewise fit to the topography generated in Section 5. Figure 6 illustrates the layer interfaces along 25° W. This figure also exposes a fundamental facet of MOM6. Namely, as in the real ocean, the model does not distinguish side from bottom. Instead, the flow feels the bottom via a bottom drag, with that property holding wherever a layer intersects the solid earth.

For diagnostics, we generally save output onto 35 z^* layers, with the remapping from native to diagnostic grid done every model timestep. We also diagnose the meridional mass transport on 64 potential density (2000 dbar) layers, again performing the remap every model time step.

7 Model initialization

We here summarize the initialization protocol followed for the p25 and p125 configurations.

7.1 p25 ocean configuration

The CM4_C192_OM4p25 piControl experiment is initialized from a 70 year spin-up run of the same model configuration (c192/OM4p25) but using a different set of runtime parameters. The spin-up run starts in year 1870 and hence produces a 1950 initial condition for all components but the ocean. The ocean's temperature and salinity are initialized from World Ocean Atlas 2018.

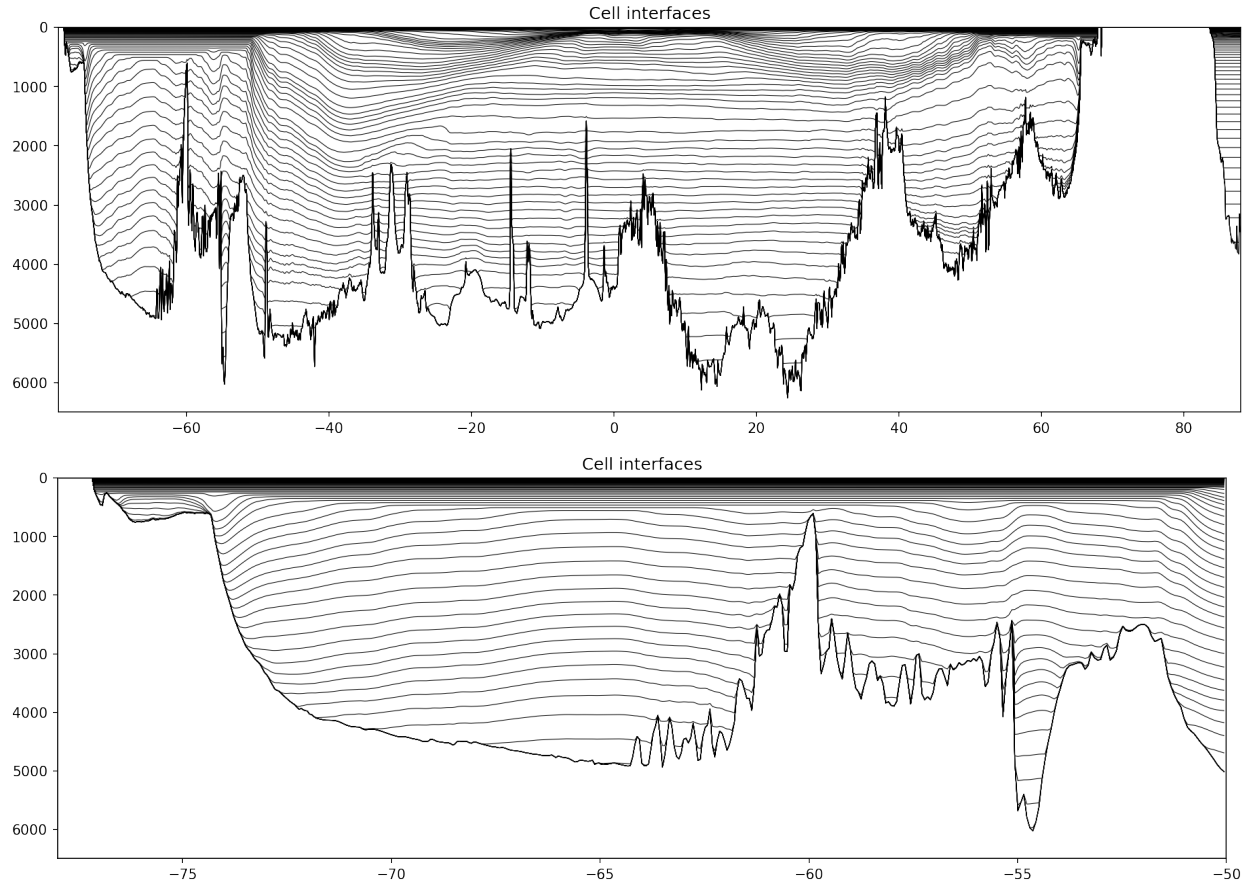

Figure 6: Layer interfaces at 25°W in the p125 configuration as time averaged over years 195-200. The upper panel shows the full latitude range whereas the lower panel focuses on a smaller region in the Southern Ocean. The horizontal layers in the upper ocean are aligned with z^* whereas the interior surfaces are aligned with potential density referenced to 2000 dbar. Also note the representation of the bottom topography is linear piecewise continuous.

7.2 p125 configuration

The CM4_C192_OM4p125 configuration, with a finer grid than the p25 configuration, has distinct land/sea masks. Initial conditions for the land model from the p25 configuration are remapped onto the p125 land/sea mask grid, with the atmospheric initial conditions left unchanged. The ocean is also initialized from World Ocean Atlas 2018.

7.3 Cryosphere

Sea-ice, icebergs and calving initial conditions for the p125 model cannot be built from the p25 model restarts. Hence, they are copied from one of the 1/8° prototypes after a 100 year long integration. Albedo parameters in the prototype are adjusted to favor Arctic sea-ice, which results in larger sea-ice extents in the p125 configuration. In the northern hemisphere, the sea-ice extent is initialized to 9.95 millions of square km in CM4_C192_OM4p25

and 11.93 millions of square km in CM4_C192_OM4p125 (20% greater). In both models, sea ice initial conditions are smaller than the typical observed values for the January Arctic sea-ice extent (15 millions of square km).

In the Southern Hemisphere, the Antarctic sea-ice extent is initialized at 7.95 millions of square km in CM4_C192_OM4p25 and 11.46 millions of square km in CM4_C192_OM4p125 (44% greater). Observed values for January are around 7 millions of square km. Figure 7 shows the spatial distribution of ice-covered regions (ice fraction greater than 15%) in the initial conditions of both model configurations.

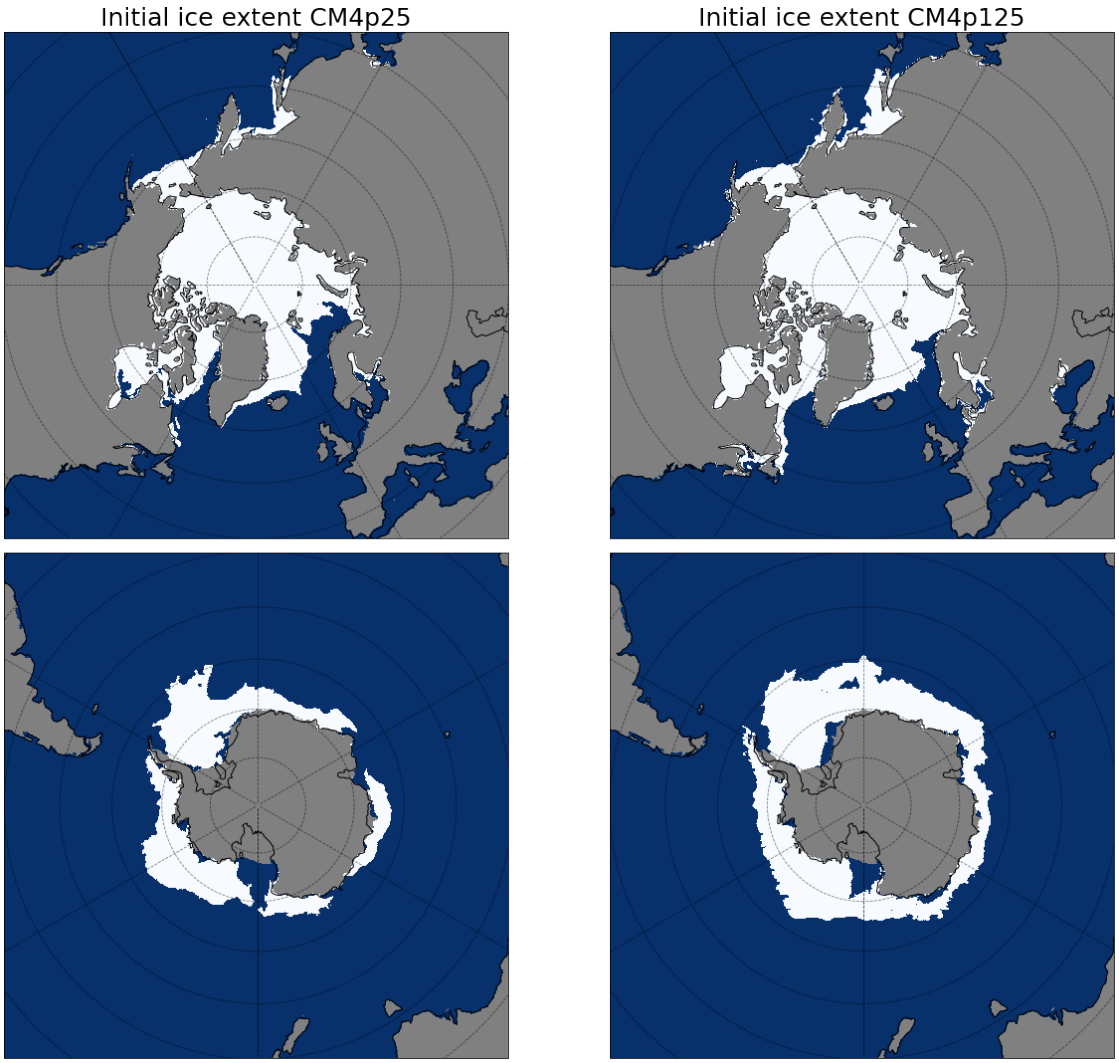

Figure 7: Sea ice initial conditions used for the p25 and p125 configurations.

8 Vertical remapping

For the vertical Lagrangian remap method used by MOM6, we require an interpolation scheme to determine the new vertical grid (see figure 3 in *Griffies et al.* (2020)). For CM4X

we use the 2nd-order accurate interpolation scheme

$$\texttt{INTERPOLATION\_SCHEME} = \texttt{P1M\_H2}, \tag{6}$$

which is also used in OM4.0 (*Adcroft et al.*, 2019).

However, from late 2020 until late 2021, we used the alternative `PPM_H4` of *White and Adcroft* (2008) and *White et al.* (2009).[4] The `PPM_H4` method is 3rd-order accurate and thus presumed to produce less spurious mixing than `P1M_H2`. Indeed, `PPM_H4` performs better than `P1M_H2` for 1-dimensional idealized tests. Nonetheless, to our dismay, `PPM_H4` produced heaps of internal spurious mixing, with Figure 8 illustrating the egregious problem with drift. Many tests using OMIP, CM4-p25, and CM4-p125 all point to `PPM_H4` as the cause of the spurious mixing, thus prompting us to return to `P1M_H2`. Odiv-191 (using `P1M_H2`) versus Odiv-183/184 (using `PPM_H4`) provide direct evidence in the p125 configuration, with the only difference being the interpolation scheme and with these experiments discussed during the Task Force meetings around 18 Nov 2021.

In Figure 9 we can see the impact of the interpolation scheme on thermal stratification in two otherwise identical JRA55 forced runs. A primary difference between the simulations is that the model with `PPM_H4` shows less stratified mode waters in the Southern hemisphere between 1000 and 2000 meters. The simulation with `P1M_H2` (panel C) maintains separation between the high-stratification and low-stratification regions, and is much more consistent with Argo observed thermal stratification over the entire North-South transect. A similar comparison between models in the CM4X development models (panels D and E) reveals nearly the same interior stratification impacts of the interpolation scheme, further pointing to this setting as the driver of ocean interior drifts.

As revealed upon running Odiv-200 for 200 years, many of the problems with Odiv-183/184 were resolved when switching to the `P1M_H2` interpolation scheme. Particular problems with long-term drift in the high latitudes were found to be related to the `PPM_H4` scheme. This experience offers a prime example of how idealized tests are not always sufficient to understand behavior in realistic models.

9 Lateral tracer advection

For lateral tracer advection (advection along coordinate surfaces), we use

$$\texttt{TRACER\_ADVECTION\_SCHEME} = \texttt{"PPM:H3"}, \tag{7}$$

which is the third order accurate piecewise parabolic method from *Huynh* (1996).

10 Coriolis and Magnus accelerations

There are a variety of numerical methods available in MOM6 for handling the Coriolis acceleration

$$\text{Coriolis + Magnus} = \frac{f+\zeta}{h}\,(\hat{\boldsymbol{z}} \times \boldsymbol{u}\,h), \tag{8}$$

[4] We first proposed using `PPM_H4` on 21 Oct 2020, largely as a means to deepen the AMOC. We used this scheme starting with Odiv-138 until around Odiv-184 near the end of 2021.

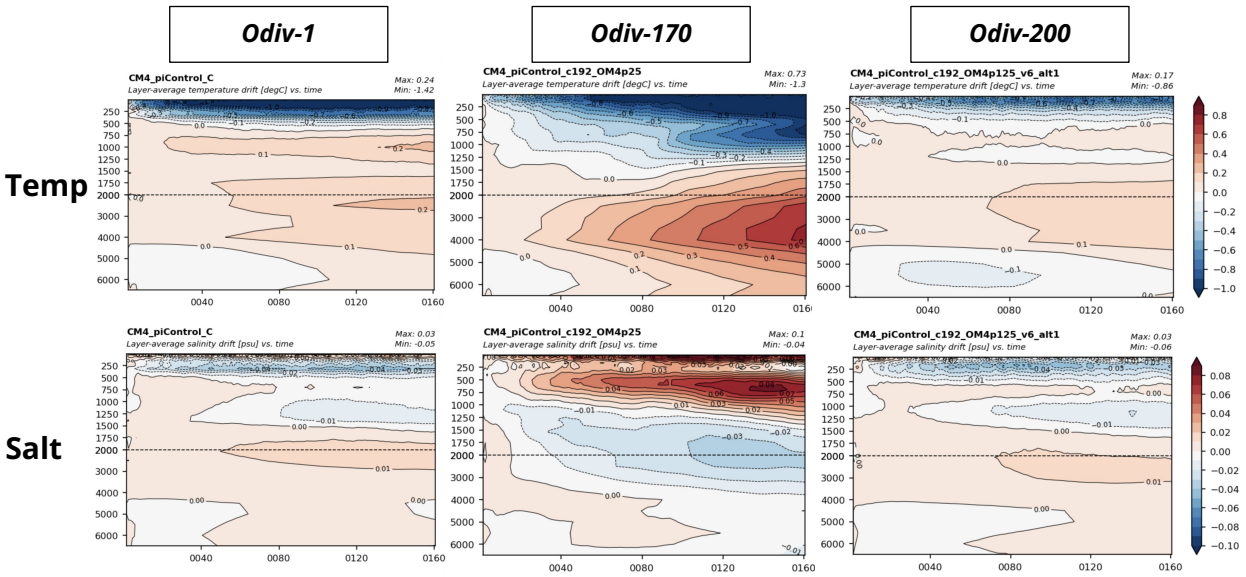

Figure 8: Time series of the annual and horizontal mean temperature relative to the first year. Left panel: CM4.0 configuration from *Held et al.* (2019), which uses `INTERPOLATION_SCHEME = P1M_H2`. Middle panel: Odiv-170, which uses `INTERPOLATION_SCHEME = PPM_H4`. Right panel: Odiv-200, which returns to the CM4.0 setting of `INTERPOLATION_SCHEME = P1M_H2`. Although there are many differences between these three simulations, numerous other experiments all point to the interpolation scheme `PPM_H4` as the cause for the huge drift in the interior found in Odiv-170 as well as all other simulations that use `PPM_H4`. We do not know if `PPM_H4` has a bug or, if no bug, then what is the reason for significantly enhanced mixing from a higher order accurate interpolation scheme.

where h is the layer thickness and ζ is the relative vorticity. The term $\zeta\hat{\boldsymbol{z}}\times\boldsymbol{u}$ is referred to as the *Magnus acceleration* in some treatments, particularly the engineering literature, whereas it is commonly referred to as the *nonlinear Coriolis acceleration* in the ocean modeling literature. Table 2 lists the suite of numerical settings found in CM4X as compared to CM4.0, with a summary of these settings given here.

- For CM4X we set `CORIOLIS_EN_DIS = True`, which means that two estimates of the layer thickness fluxes are used to estimate the Coriolis + Magnus accelerations, and the one that dissipates energy relative to the other one is used. In CM4.0 this parameter was set False.

- In CM4.0 and CM4X we set `CORIOLIS_SCHEME = "SADOURNY75_ENSTRO"`, which is based on the enstrophy conserving scheme detailed in *Sadourny* (1975).

- In CM4.0 and CM4X we set `BOUND_CORIOLIS = True`, which means that the Coriolis terms at u-points are bounded by the four estimates of $(f + \zeta)v$ from the four neighboring v-points, and similarly at v-points. This option would have no effect on the SADOURNY Coriolis scheme if it were possible to use centered difference thickness fluxes.

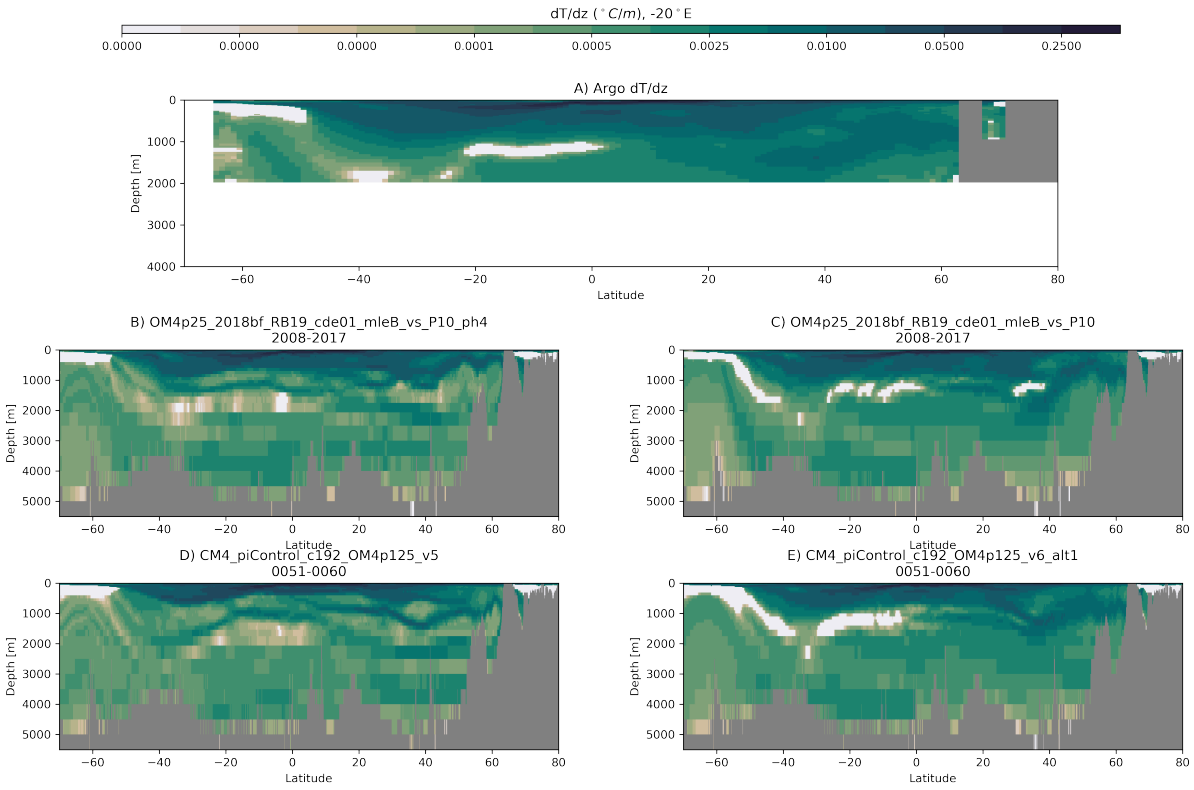

Figure 9: Comparing the meridional transect of ocean thermal stratification at -20°E between Argo (panel A) and four MOM6 based ocean models. Panels (B) and (C) compare the impact of the interpolation scheme in two otherwise identical 1/4 degree MOM6 models forced with JRA55-do reanalysis, where panel (B) uses `INTERPOLATION_SCHEME` = `PPM_H4` and panel (C) uses `INTERPOLATION_SCHEME` = `P1M_H2`. Panels (D) and (E) compare two 1/8 degree coupled model runs with several differences, including panel (D) using `INTERPOLATION_SCHEME` = `PPM_H4` and panel (E) using `INTERPOLATION_SCHEME` = `P1M_H2`. Note that closer agreement with Argo for the panels using `INTERPOLATION_SCHEME` = `P1M_H2`.

- In CM4.0 and CM4X we set `KE_SCHEME = "KE_ARAKAWA"`, which determines the discretization for acceleration from the kinetic energy gradient.
- In CM4.0 and CM4X we set `PV_ADV_SCHEME = "PV_ADV_CENTERED"`, which determines the discretization of PV advection as per the centered scheme of *Sadourny* (1975).

11 Penetrative shortwave and chlorophyll

Unlike the earth system model ESM4 detailed by *Dunne et al.* (2020), we here do not make use of a prognostic biogeochemistry model. Consequently, as in *Adcroft et al.* (2019), use a monthly climatology (from years 1997-2010) of chlorophyll-a measurements taken from

SCHEME	CM4.0	CM4X
NOSLIP	False	False
CORIOLIS_EN_DIS	False	True
CORIOLIS_SCHEME	SADOURNY75_ENSTRO	SADOURNY75_ENSTRO
BOUND_CORIOLIS	True	True
KE_SCHEME	KE_ARAKAWA	KE_ARAKAWA
PV_ADV_SCHEME	PV_ADV_CENTERED	PV_ADV_CENTERED

Table 2: Summary of the various numerical settings associated with the Coriolis and Magnus accelerations.

Hu et al. (2012). We display the January chlorophyll-a concentration in Figure 10. The cholorophyll-a concentration is then used to modify the penetrative shortwave radiation in the upper ocean, following the optics scheme of *Manizza et al.* (2005).

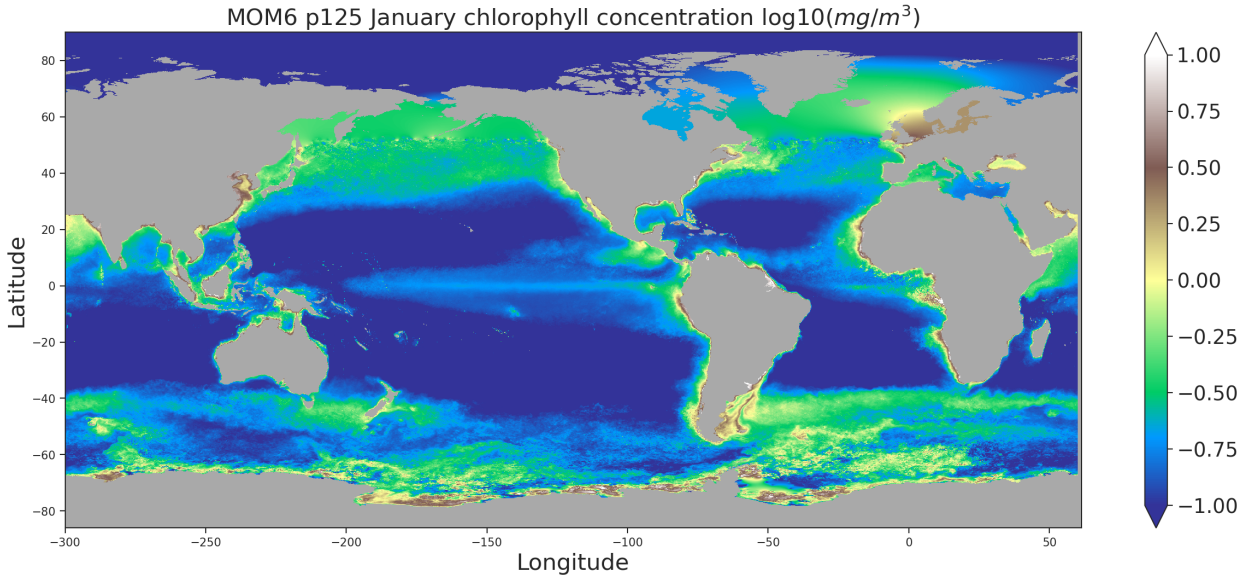

Figure 10: January chlorophyll concentration as used for the p125 configuration.

12 Geothermal heating

The geothermal heat flux is taken from *Huw Davies* (2013), with a global area average of 0.095 W m^{-2}. This field is static and applied as a bottom boundary condition on the temperature equation.

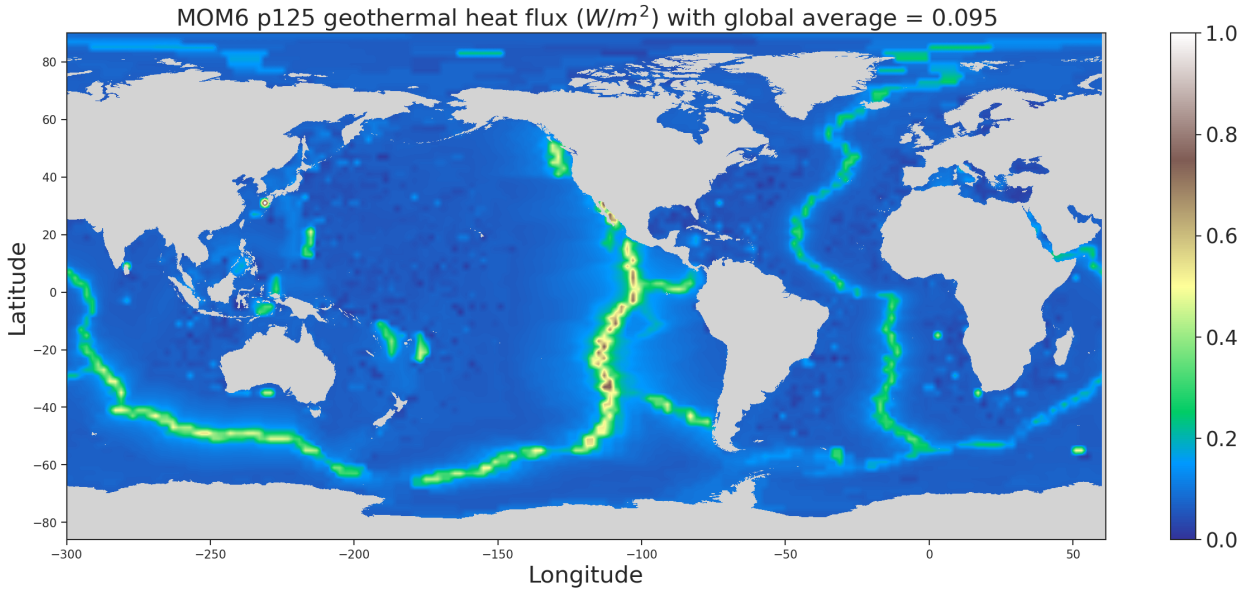

Figure 11: Ocean bottom geothermal heating for p125 MOM6 model configuration, as taken from *Huw Davies* (2013).

13 Equation of state

We make use of the *Wright* (1997) equation of state and use a heat capacity as a global constant

$$C_p = 3992 \text{ J K}^{-1} \text{ kg}^{-1}. \tag{9}$$

We also assume the potential temperature field, $\theta(\boldsymbol{x}, t)$, satisfies a conservative advection-diffusion equation with no interior sources

$$\frac{\partial \theta}{\partial t} + \nabla \cdot (\boldsymbol{v}\, \theta) = -\nabla \cdot \boldsymbol{J}, \tag{10}$$

where $\nabla \cdot \boldsymbol{v} = 0$ as per the Boussinesq approximation, and $\boldsymbol{J}$ is the subgrid scale flux. According to *McDougall et al.* (2021), we are obliged to interpret θ as the Conservative Temperature, Θ.

Question

What temperature is passed to the atmosphere for the SST? Do we just pass it $\theta(k = 1)$ or is there something else?

14 Diapycnal diffusivities

We here summarize the various components that contribute to the diapycnal diffusivity. Figure 12 shows the 10-year mean net diapycnal diffusivity along 25°W from the p125 configuration. This diffusivity is built from a number of distinct diffusivities that arise from a variety of mixing processes.

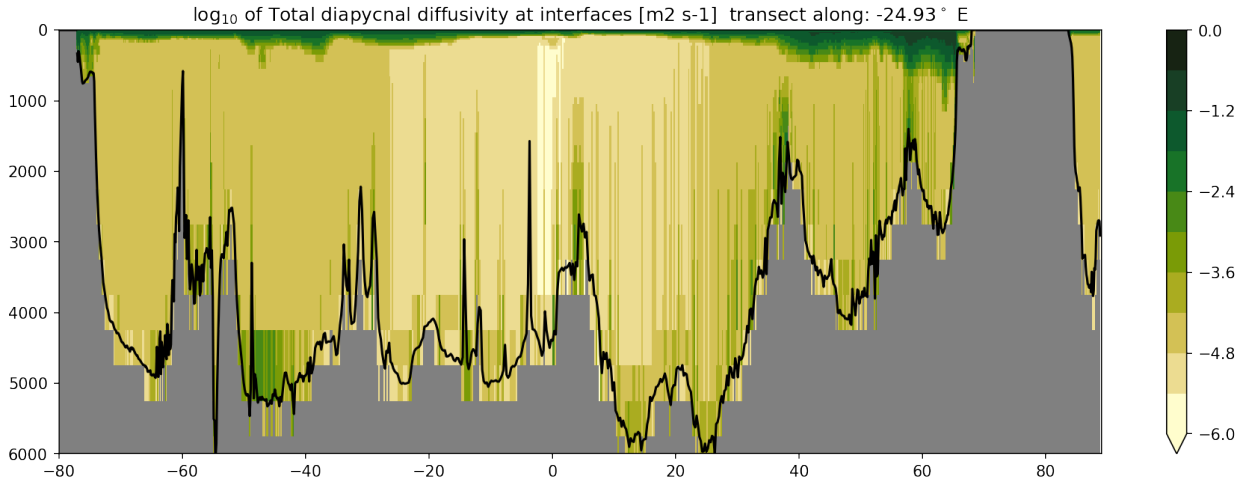

Figure 12: Meridional-vertical slice along 25°W of a 10-year mean bottom boundary layer diffusivity (log in $m^2\ s^{-1}$) from the p125 configuration from the downsampled grid. The diagnostic table entry for this field is `Kd_interface`. The black line is the model bottom topography.

14.1 Static background diffusivity

Figure 13 shows the static background diapycnal diffusivity used in CM4X. The profile is depth-independent and has a latitudinal dependence given by *Henyey et al.* (1986).

The following discussion is from the Odivision meeting on 09 Sep 2020:

- Is Arctic SSS high biases from too much mixing by Henyey background diffusivity?
  - Mike noted that this salty bias appeared in the CM4 development when enabled Henyey mixing.
  - Alistair noted that there is an opposite bias in OM4, though this might be corrupted due to the SSS restoring.
  - Sonya noted that Yankovsky's analysis suggests there is too much mixing around the edges of the Arctic. She also noted that there should be basically not background mixing in center of the Arctic.
  - Bob noted that Henyey is an empirical fit to the tropical Pacific. It was not considering Arctic.
  - Task Force concluded on 23 Sep 2020 that research is needed to get a suitable mixing scheme for the Arctic. Developing the new mixing scheme is an Odivision task that is outside the scope of current TF deliberations.
  - Update as of March 2022: Brandon has initiated this research, in concert with questions about the tropical thermocline and vertical gridding.

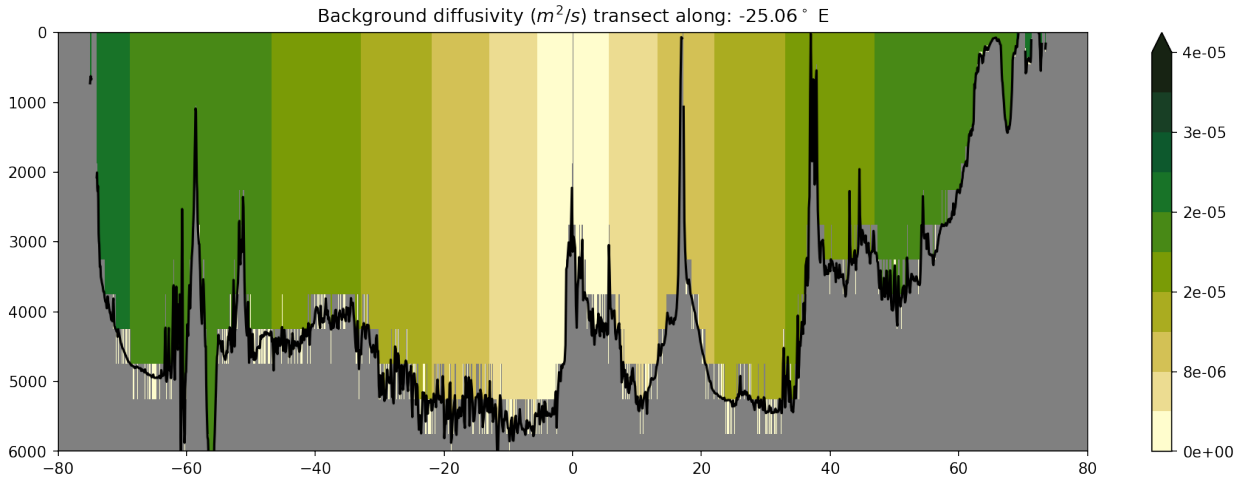

Figure 13: Meridional-vertical slice of the background diffusivity (m^2 s^{-1}) from the p125 configuration from the downsampled grid. This diffusivity was inferred from the other diffusivities, which is not possible everyhere, hence the corrupted values near boundary layers.

14.2 EPBL upper ocean boundary layer scheme

The upper ocean boundary layer scheme is based on *Reichl and Hallberg* (2018), and we include the *Reichl and Li* (2019) extension that parameterizes effects from Langmuir turbulence. The settings are updated to more sanctioned values than used in *Adcroft et al.* (2019), resulting in a slight increase in mixing. Figure 14 shows the 10-year mean ePBL diffusivity along 25°W.

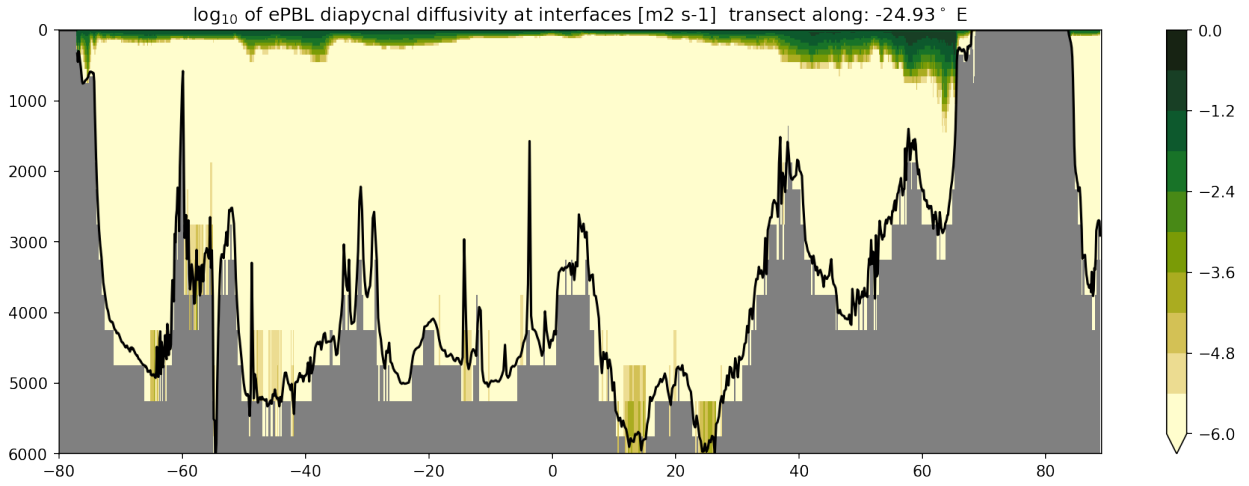

Figure 14: Meridional-vertical slice along 25°W of a 10-year mean ePBL diffusivity (log in m^2 s^{-1}) from the p125 configuration from the downsampled grid. The diagnostic table entry for this field is `Kd_ePBL`.

14.3 Shear-driven scheme

Shear driven mixing is parameterized according to the *Jackson et al.* (2008) scheme. A modification has been implemented for computing the Richardson number that removes the traditional horizontal noise in the tropics found by the earlier methods. This modification is realized by setting the logical `VERTEX_SHEAR = True`, in which the calculations of the shear-driven mixing is performed at the cell vertices. Figure 15 shows the 10-year mean shear-driven diffusivity along 25°W.

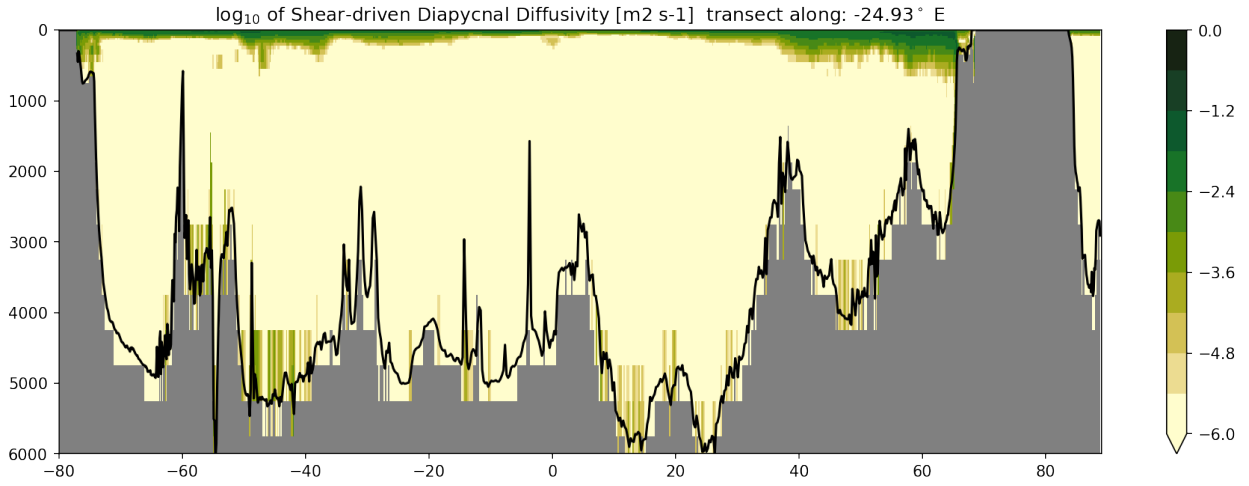

Figure 15: Meridional-vertical slice along 25°W of a 10-year mean shear-driven diffusivity (log in $m^2\ s^{-1}$) from the p125 configuration from the downsampled grid. The diagnostic table entry for this field is `Kd_shear`.

14.4 Bottom boundary layer and bottom drag

As detailed in Section 2.2.4 of *Adcroft et al.* (2019), we make use of a quadratic bottom drag in the form

$$\boldsymbol{F}_{\text{drag}} = -\rho_0\, C_{\text{d}}\, \boldsymbol{u}\, \sqrt{\boldsymbol{u}^2 + u^2_{\text{tides}}}, \tag{11}$$

where $\boldsymbol{u}$ is the horizontal velocity within the ocean domain adjacent to the bottom, $C_{\text{d}} = 0.003$ is a constant bottom drag coefficient, $u_{\text{tides}} = 0.1$ m s^{-1} is a constant background tide speed, and $\rho_0 = 1035$ kg m^{-3} is the reference density for the Boussinesq approximation. Following the parameterization of *Legg et al.* (2006), 20% of the mechanical energy dissipated from bottom drag is provided as a source for diapycnal mixing in the bottom boundary layer. Figure 16 shows the 10-year mean bottom boundary layer diffusivity along 25°W.

14.5 Internal tide induced mixing

Mixing from breaking internal tides is an important piece to the parameterized mixing of tracers and momentum in CM4. The parameterization follows the methods of *Melet et al.*

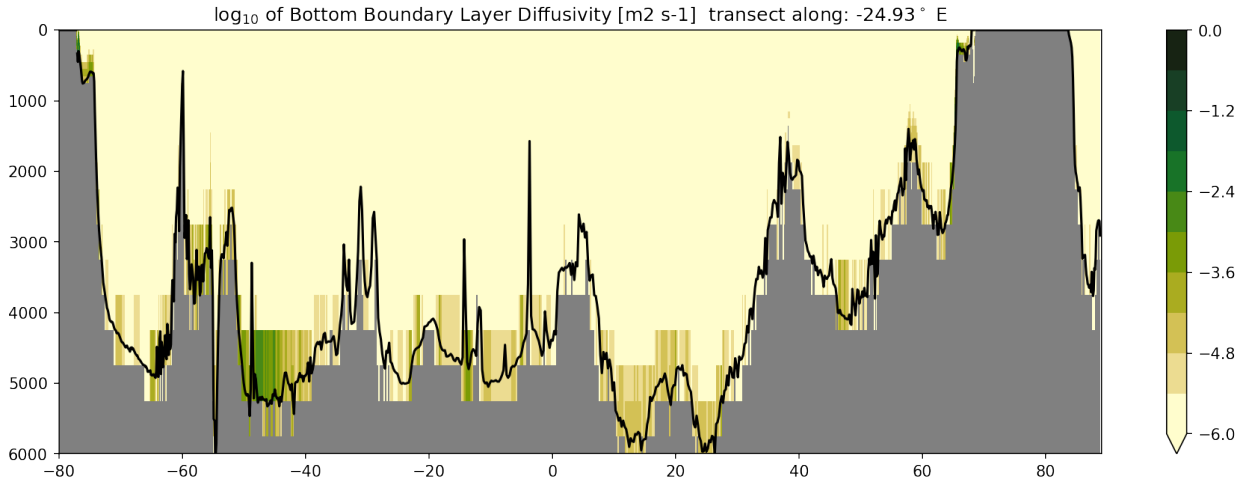

Figure 16: Meridional-vertical slice along 25°W of a 10-year mean bottom boundary layer diffusivity (log in $m^2\ s^{-1}$) from the p125 configuration from the downsampled grid. The diagnostic table entry for this field is `Kd_BBL`.

(2013). This mixing requires input from the variance of subgrid bottom topography and from tide amplitudes. We here document these two static input fields.

Topography variance

The following repository hosts the code for generating the variance field, h2, used in the parameterized tidal induced mixing scheme

```
https://github.com/nikizadehgfdl/ocean_model_topog_generator/tree/master/OMtopogen
```

The code is inside the Python script `create_topog_refinedSampling.py`, and it computes the roughness by fitting a plane to the topography contained in `ocean_topog.nc` (Section 5.4), and then calculating the slope of the plane. Figure 17 shows the h2 field for the p125 model, with this field contained in the file `ocean_topog.nc` from Section 5.4.

Amplitude of tides

We make use of the TPX09 version of the Oregon State University barotropic shallow water tide model that uses the methods from *Egbert and Erofeeva* (2002), and which is available from download at this website

```
https://www.tpxo.net/global/tpxo9-atlas
```

This model has a 1/30° grid spacing and we make use of these 8-harmonics: M2, S2, N2, K2, K1, O1, P1, Q1. The following repositories host the code to perform the interpolation of the tide amplitude onto the p25 and p125 MOM6 grids:

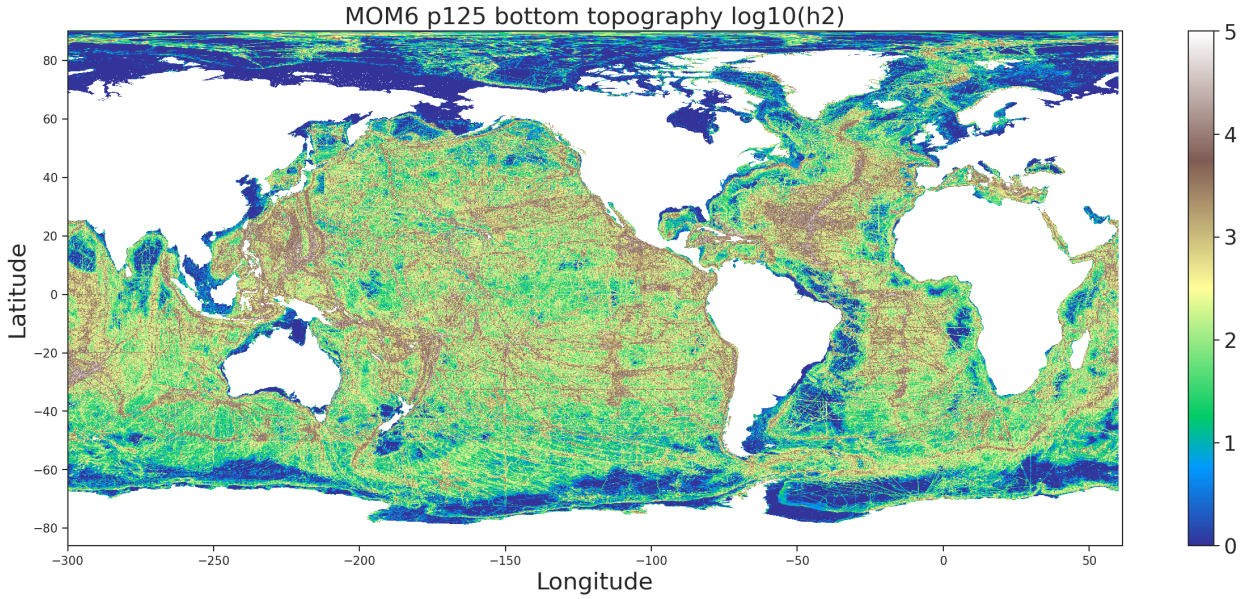

Figure 17: Log10 of the h2 field (squared meters) for the bottom topography in the p125 configuration, with this field used in the tide-induced mixing parameterization. It is notable that straight lines appear from ship data, particularly visible in the high latitudes.

```
https://github.com/raphaeldussin/OM4p25_tideamp
https://github.com/raphaeldussin/OM4p125_tideamp
```

Figure 18 shows the tide amplitude for the p125 grid. Once the tide amplitude has been interpolated to the model grid, we tune the global deep ocean tide dissipation to be roughly 1 TW based on World Ocean Atlas bottom stratification. This tuning is performed separately in the p25 and p125 configurations by setting values for the characteristic topographic wavenumber responsible for the generation of internal waves (*St. Laurent et al.*, 2002; *Simmons et al.*, 2004). The recommended value from *St. Laurent et al.* (2002) is $\kappa = 2\pi/10$ m^{-1}. We here take the following values, based on tuning the diagnostics `TKE_tidal` and `TKE_itidal`

$$\texttt{KAPPA\_H2\_FACTOR} = 0.93 \text{ m}^{-1} \qquad \text{p25 configuration} \tag{12a}$$

$$\texttt{KAPPA\_H2\_FACTOR} = 6.4 \text{ m}^{-1} \qquad \text{p125 configuration.} \tag{12b}$$

However, as per the Task Force discussion on 07 Oct 2020, it seems that `KAPPA_H2_FACTOR` = 6.4 m^{-1} gives roughly 1 TW dissipation for the p25 configuration, so that the 0.93 value from the CM4.0 configuration might best be changed.

14.5.1 Sample diffusivity

Figure 16 shows the 10-year mean internal tide generated diffusivity along 25°W.

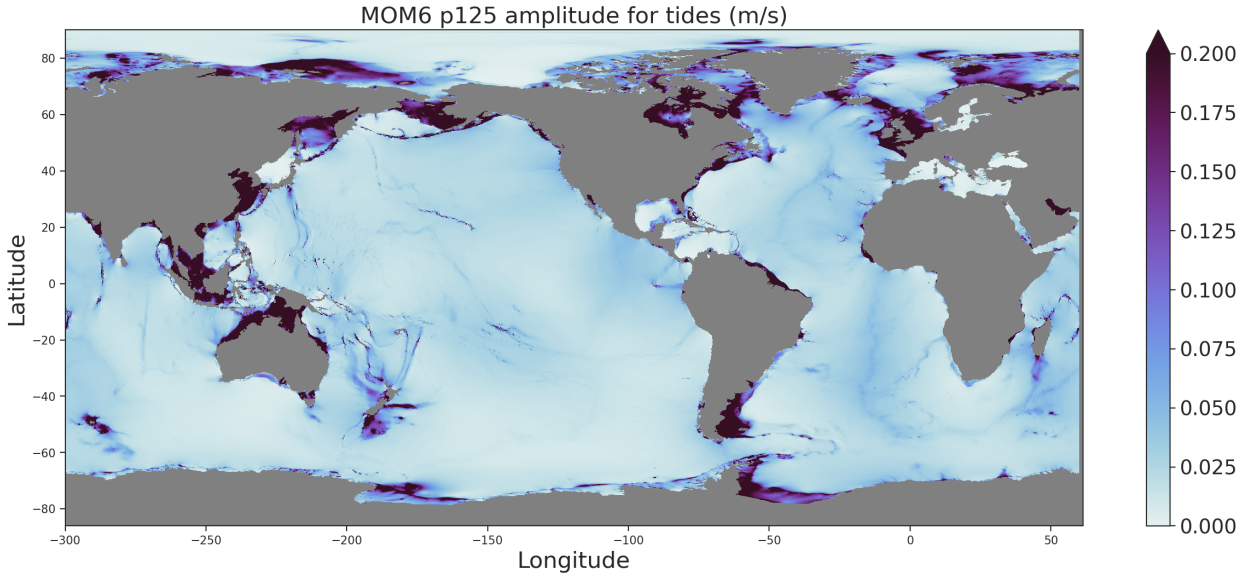

Figure 18: Amplitude (m/s) of the tides used for the tidal included mixing in MOM6 for the p125 configuration.

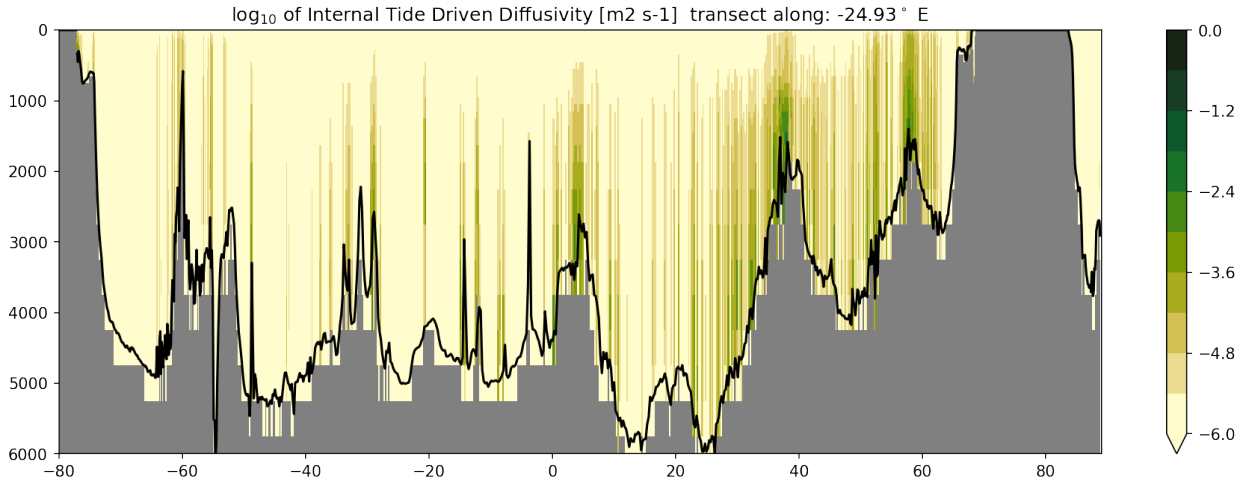

Figure 19: Meridional-vertical slice along 25°W of a 10-year mean internal tide diffusivity (log in m^2 s^{-1}) from the p125 configuration from the downsampled grid. The diagnostic table entry for this field is `Kd_itides`.

15 Mixed layer eddy (MLE) restratification

The mixed layer eddy (MLE) restratification scheme is based on *Fox-Kemper et al.* (2008) and *Fox-Kemper et al.* (2011), who provide a parameterization of the mixed layer baroclinic instability as studied by *Boccaletti et al.* (2007). Details of the MOM6 implementation of this scheme can be found in this MOM6 read-the-doc, whereas Section 2.2.2 of *Adcroft et al.* (2019) outlines the implementation for OM4.0. We closely follow the OM4.0 approach, with one parameter modification noted in Table 3. Notably, this implementation makes

use of the EPBL boundary layer depth rather than the more traditional mixed layer depth (MLE_USE_PBL_MLD = True) as a measure of the depth over which the MLE scheme acts.

In the absence of a mesoscale eddy closure, as in the p125 and p125 configurations, the MLE scheme is a huge tuning knob for restratification and ocean ventilation. Hence, the scheme plays a large role in ocean heat uptake and the mixed layer depth, along with the SST. These fields were our primary target when tuning the MLE scheme. There are two parameters in this scheme that we tested. The MLE_FRONT_LENGTH sets the size of submesoscale fronts in the upper ocean boundary layer. The strength of the restratification is inversely proportional to the size of the front, with a stronger restratification for smaller fronts. The parameter MLE_MLD_DECAY_TIME sets the timescale for a running time mean filter applied to the mixed layer depth. This time filtering was detailed in Section 2.2.2 of *Adcroft et al.* (2019), and it was motivated as a means to low-pass filter the rapidly varying planetary boundary layer over which the MLE scheme acts.

We tested (non-exhaustive tests) a front length of 1000 m and 2000 m, yet found relatively little sensitivity to this parameter relative to the OM4.0 setting of 500 m, thus prompting us to retain 500 m. In contrast, the model heat uptake and SST are sensitive to the time for the low pass time filter. Increasing the decay time increase the strength of the restratification since the longer time filter allows the MLE scheme to remain enabled for a longer period of time. In general, the upper ocean warms when the MLE restratification is strengthened (heat remains in the upper ocean), and the upper ocean cools when the MLE restratification is weakened (heat can be pumped into the ocean interior). In addition to heat uptake, we monitored the mixed layer depth and SST when testing these parameters. Table 3 lists the chosen settings.

For the 1850 piControl simulation in CM4.0, the SST cools, as expected for a pre-industrial simulation. However, the cooling was quite large, so much so that the model failed to warm sufficiently to match present-day properties. Since SST is a primary field for coupled modeling, we tuned the MLE to provide a very strong restratification to partially counteract the upper ocean cooling. Evern with this strong restratification, the upper ocean cooled and that led to further heat input to the ocean that warmed the ocean interior, thus leading to a rather large global mean temperature rise.[5] By tuning the MLE scheme to be very strong, it is arguable that the OM4.0 settings result in far more restratification than originally intended by *Fox-Kemper et al.* (2008) and *Fox-Kemper et al.* (2011). Hence, in developing CM4X we attempted to reduce the strength of the scheme. We did so by increasing the front length, which, as mentioned above, did not show much sensitivity thus prompting us to keep the same value as OM4.0. We instead relied on time filtering time scale, reducing it from 30 days to 20 days. We also felt that this change was partially motivated from a model development perspective since the p125 ocean has stronger mesoscale eddies, thus helping with upper ocean restratification and so providing the means to reduce the strength of the MLE scheme. Table 3 summarizes the chosen parameter settings for the MLE scheme.

[5] More discussion on this point needed.

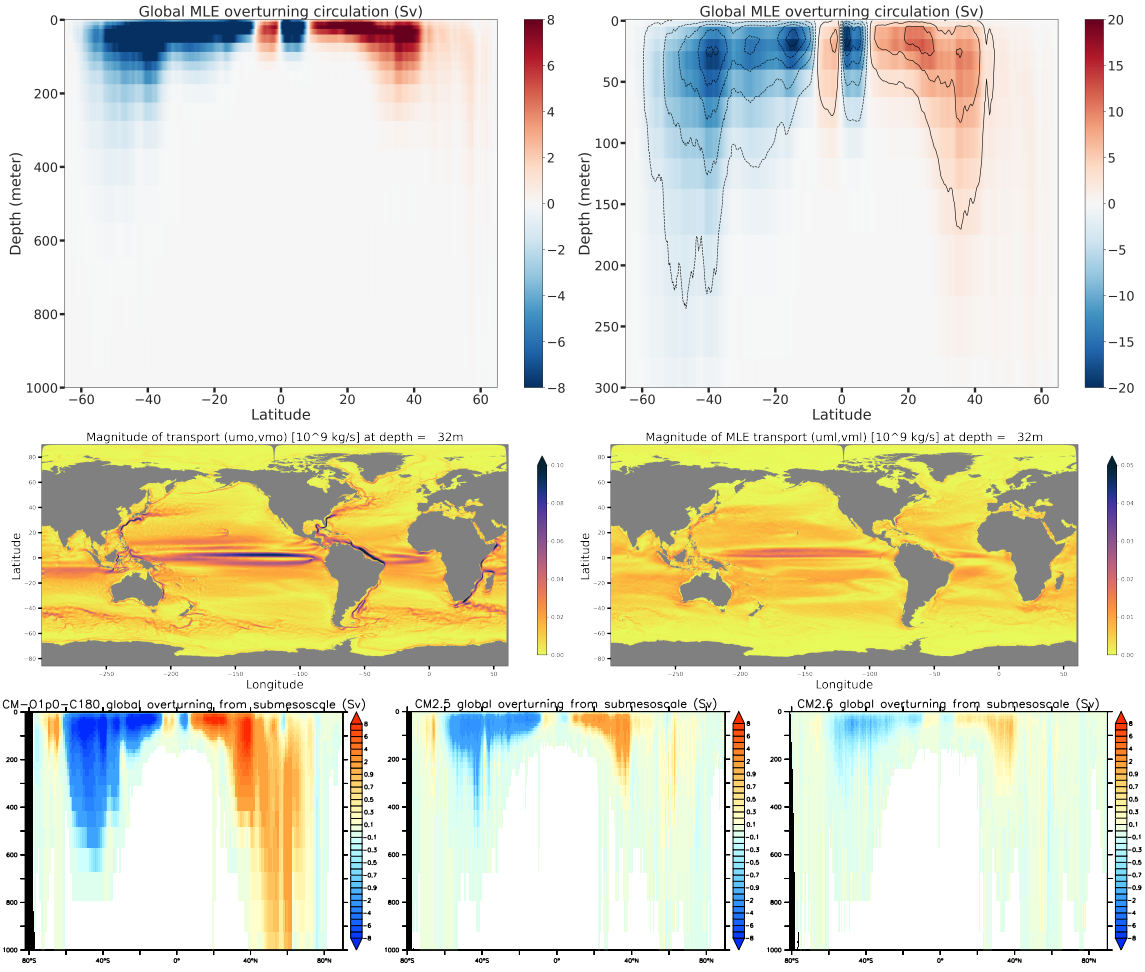

Figure 20: Meridional-depth overturning for the global ocean based on the MLE transport. The upper left panel shows the color range according to the CM2-O suite shown in the lower panels, whereas the upper right panel shows a range more compatible with the values realized, and with a focus on the upper ocean. The middle left shows the magnitude of the horizontal mass transport at 32 m depth arising from the resolved flow plus the MLE scheme, whereas the middle right shows that transport just from the MLE scheme. Note in particular the relatively large MLE contribution in the northern equatorial region. For comparison with the upper panels from CM4X, we show in the lower panels the meridional-depth overturning for the global ocean based on the MLE transport from the CM2-O suite of *Griffies et al.* (2015). The left panel is from CM2-1deg, middle from CM2.5, and right from CM2.6. Note the much smaller values in CM2.5 and CM2.6 relative to CM4X shown in the upper panls.

16 Sea ice and land ice albedos

We explored a series of sea ice albedo and land albedo settings through the development process. The sea ice albedo tunings were motivated by biases in Arctic sea ice thickness and summer Arctic sea ice extent. However, as of Odiv-206 (31 March 2022) we returned

MODEL	MLE_FRONT_LENGTH	MLE_MLD_DECAY_TIME
CM4.0	500 m	2.592×10^6 s = 30 days
CM4X	500 m	1.728×10^6 s = 20 days

Table 3: Summary of the key MLE parameters as used in CM4.

MODEL	ICE_DELTA_EDD_R_ICE	ICE_DELTA_EDD_R_SNOW	ICE_DELTA_EDD_R_POND
Odiv-210	1.0	1.0	1.0
Odiv-209	1.0	1.0	1.0
Odiv-207	1.0	1.0	1.0
Odiv-206	1.0	1.0	1.0
Odiv-200	0.0	0.0	0.0
Odiv-1 (CM4.0)	1.0	1.0	1.0
ESM4.1	1.5	1.5	1.5
SPEAR	0.0	0.0	0.0

Table 4: Summary of the sea ice albedo settings. Albedos are in units of observed standard deviations relative to observed mean values (*Briegleb and Light*, 2007). The Odiv-209 settings are the same as used in CM4.0.

to the CM4.0 settings as summarized in Table 4.

The Odiv-200 configuration suffered from the following issues:

- Arctic sea ice that was too thin and biased low in summer;
- Antarctic sea ice that was biased low in summer;
- Systematic model drift towards a weakening Antarctic circumpolar current and weakening Antarctic Bottom Water (AABW) transport.

These biases motivated tuning the sea ice albedo parameters, which were increased from values of 0.0 in Odiv-200 to values of 1.0 in Odiv-206. In addition to the anticipated increase

MODEL	F_ISO_WARM_ON_GLACIER	F_ISO_COLD_ON_GLACIER
Odiv-210	0.77, 0.58	0.92, 0.73
Odiv-209	0.77, 0.58	0.92, 0.73
Odiv-207	0.77, 0.58	0.92, 0.73
Odiv-206	0.77, 0.43	0.92, 0.68
Odiv-200	0.77, 0.43	0.92, 0.68
Odiv-1 (CM4.0)	0.77, 0.43	0.92, 0.68
ESM4.1	0.77, 0.58	0.92, 0.73
SPEAR	0.77, 0.43	0.92, 0.68

Table 5: Summary of the glacier albedo settings, listing the values for (Visible, Near IR) radiation and warm/cold surfaces. The Odiv-209 and Odiv-210 settings are the same as used in ESM4.1.

of sea ice thickness and summer sea ice extent, this albedo tuning was also motivated by the expectation that cooling the Southern Ocean surface would encourage intermittent oceanic convection and production of AABW (*Delworth et al.*, 2020; *Zhang et al.*, 2021). Odiv-206 showed improvements in Arctic and Antarctic sea ice and also showed some improvements in the production of dense waters on the Antarctic continental shelves, however this dense water production was still biased low relative to CM4.0 (Odiv-1).

The above results motivated an additional sensitivity experiment (Odiv-207), in which the land ice albedos were increased to ESM4.1 values (see summary in Table 5), which had been found in ESM4.1 development to enhance Southern Ocean ventilation due to cooling of the Southern Ocean surface. Odiv-207 showed a substantial improvement in Southern Ocean ventilation, thus supporting these sea ice and land ice albedos for a new PI-control run, Odiv-209.

Note that the ESM4.1 documentation paper *Dunne et al.* (2020) states that "we had to increase the near infrared albedo of snow on glaciers to a value of 0.82." This value of 0.82 is different than the values in Table 5 because it refers to the total ratio of shortwave up to shortwave down, which is an emergent property value of the simulation. Thus, it would be more appropriate for *Dunne et al.* (2020) to say "we found that we had to increase the near infrared albedo of snow on glaciers to obtain an overall shortwave albedo value of 0.82 for these regions..." (John Dunne, personal communication).

17 Bug fix for Arctic bipolar fold

During the development process (in Sept 2022) a numerical error was identified along the bipolar grid fold in the Arctic Ocean (see Fig. 21). This error was found to be present in all MOM6/SIS2 model configurations that were checked, including CM4p125, CM4p25, CM4.0, ESM4.1, SPEAR, coupled slab ocean configurations, and ice-ocean configurations. The numerical error occurs along the half of the bipolar fold that extends from the geographic North Pole to the grid pole located in Russia. The error is most visibly present in zonal and meridional sea ice velocity fields, but also creates artifacts in sea ice thickness and concentration fields and upper ocean fields.

After investigation, it was found that a bug fix for the bipolar fold error was made in SIS2 in September 2018. See

`https://github.com/NOAA-GFDL/MOM6/commit/0e96fbaede18bd97f4252dd40c6eeacf54d177c5`

for details of this bug fix. As part of this bug fix, a runtime flag

```
USE_TRIPOLAR_GEOLONB_BUG
```

was added to the code. Setting this flag to

```
USE_TRIPOLAR_GEOLONB_BUG = True
```

retains the bug, allowing for backward compatibility with older model runs such as CM4.0. The default setting is

```
USE_TRIPOLAR_GEOLONB_BUG = False
```

which fixes the bug. Odiv-209 and Odiv-210 (as well as earlier experiments in the CM4_HighRes development suite) used values that were consistent with the code used for Odiv-1. Specifically, a parameter setting of `USE_TRIPOLAR_GEOLONB_BUG=False` was used for MOM6 and `USE_TRIPOLAR_GEOLONB_BUG=True` was used for SIS2. The values for MOM6 and SIS2 are different because the original bug was present in SIS2 but coded correctly in MOM6. It was found that setting the SIS2 runtime flag to `False` removed the bipolar numerical error (see Fig. 22).

After identifying this bug fix, additional simulations were performed to evaluate the impact of this sea ice bug on Arctic climate. It was found that...(Add text here). Based on these findings, the following strategy was chosen for extending the CM4p125 and CM4p25 simulations. (Add text here)

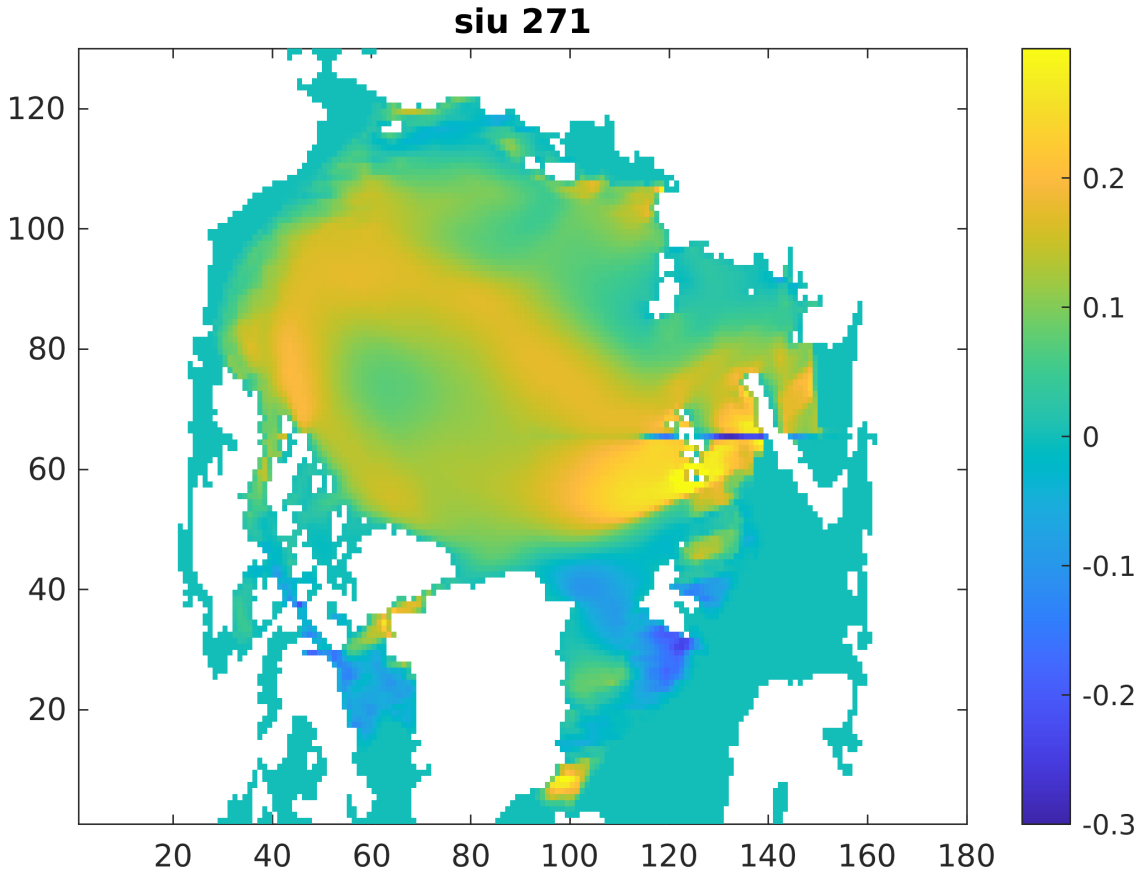

Figure 21: Example of the Arctic bipolar fold bug. Plotted is the zonal sea ice velocity from a JRA55do-forced ice-ocean SPEAR run on day 271 of 1958. No plotting software has been used in generating this figure. For visualization purposes, the data has been folded across the bipolar fold using the same method that the model employs to make halo updates across the bipolar fold.

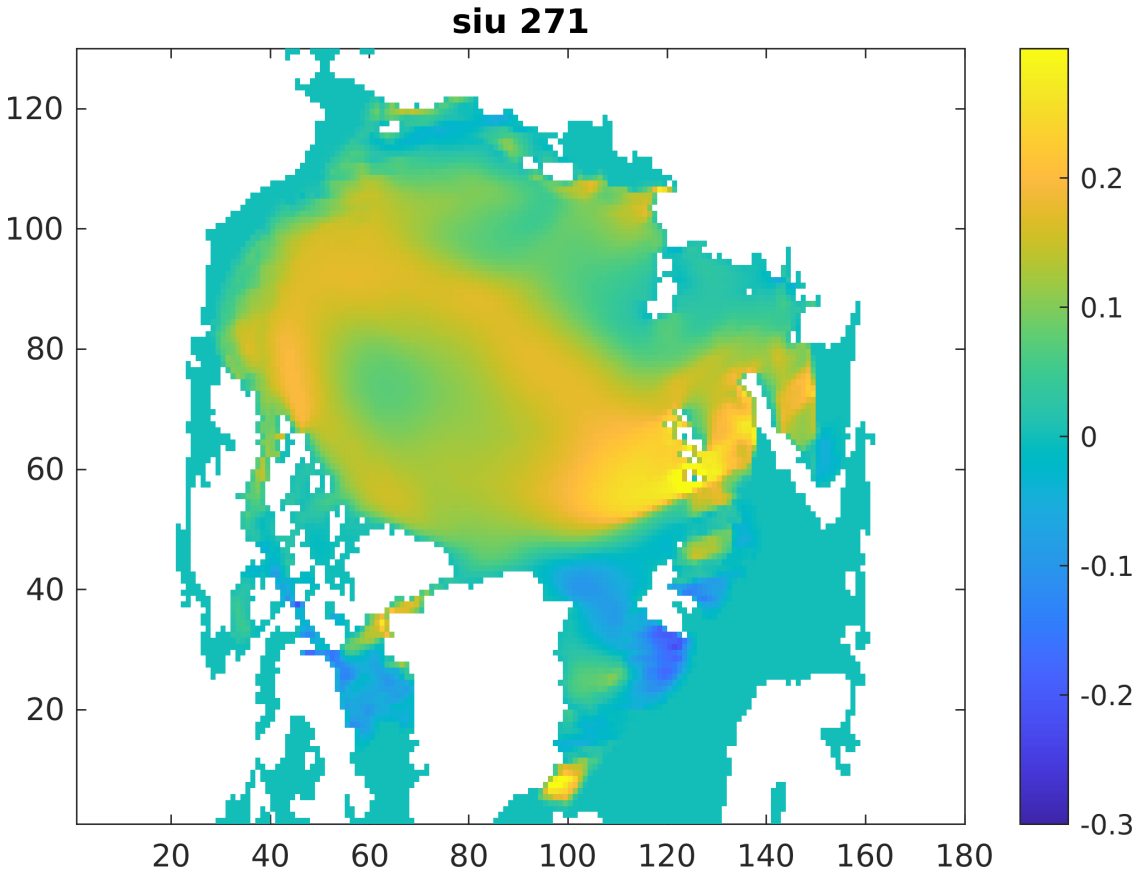

Figure 22: Example of the Arctic bipolar fold after the bug fix. Plotted is the zonal sea ice velocity from a JRA55do-forced ice-ocean SPEAR run on day 271 of 1958. No plotting software has been used in generating this figure. For visualization purposes, the data has been folded across the bipolar fold using the same method that the model employs to make halo updates across the bipolar fold.

18 Density bins to diagnose the MOC

Figure 23 summarizes issues related to ρ_{2000} density bins used for the diagnosing the meridional overturning circulation (MOC). Issues were first seen when noting the extremely light penetration of the overturning cells in the tropics using the 64-layer density bins, with the 64-layer densities chose to emulate the prognostic model. Whereas the model transitions to z-coordinate in the light density classes found in the mixed layer, the 64-layer diagnostic grid remains poorly sampled in the light classes, thus leading to misleading overturning in the tropics. In contrast, the 35-layer binning (used for CM4.0) does fine in the tropics. However, the 35-layer binning is too coarse in the deep ocean and so compromises the deeper cells, particularly in the Southern Ocean.

We tested two more binnings to resolve the above issues with the 64-layer and 35-layer classes. One uses 62-layers and another 69-layers, both of which were seen to be roughly the same, and both resolving issues with the light and dense overturnings. To reduce output volume we chose the 62-layer binning as the standard binning used for the

simulations starting Oct 2022. However, to maintain consistency across earlier runs we save annual means for the 35-layer and 64-layer bins.

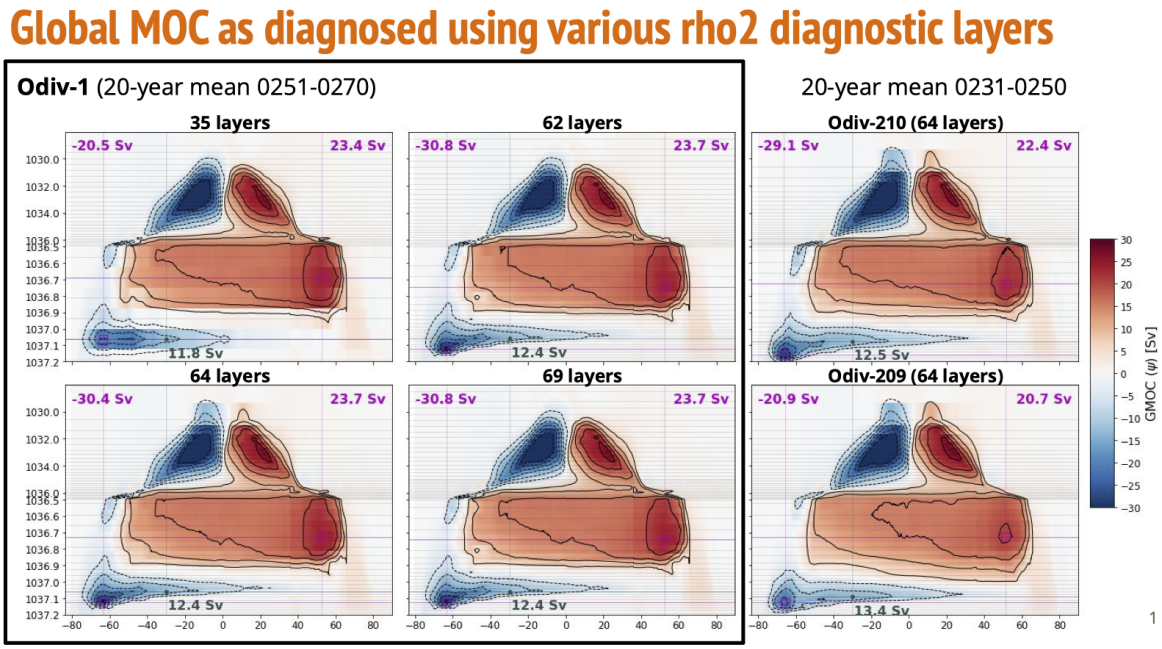

Figure 23: Examples of the global meridional-ρ_{2000} overturning circulation. In each panel, the horizontal lines indicate the boundaries of the density bins used for binning the vmo transport. The four panels on the left (enclosed in the black box) were generated from Odiv-1 using the same data and binned using different ρ_{2000} bins (35, 62, 64, and 69 layers). The panels on the right were generated using the same 64-layer ρ_{2000} bins for Odiv-209 and Odiv-210. All figures using the 64-layer binning show tropical cells that extend into very light density classes, with this feature an artefact of the extremely coarse bins in the lighter classes. All other diagnostics show no problem with the lighter density classes due to there being finer density bins in the light waters. In the deep ocean, the 35-layer binning shows problems with the the Southern Ocean. The 62-layer binning was found to be most suitable.

19 Experiments analyzed in the JAMES paper

Here are the experiments analyzed in the JAMES manuscript according to their Dora numbers.

19.1 CM4.0

Odiv-001: piControl

The piControl for CM4.0 has been run for 650 years.

Odiv-002: historical

The historical for CM4.0 runs from 1850 to 2014.

SSP585

The SSP585 for CM4.0 is available at

```
/archive/oar.gfdl.cmip6/CM4/warsaw_201803_om4_v1.0.1
/CM4_Scenario_ssp585/gfdl.ncrc4-intel16-prod-openmp
```

19.2 CM4X-p25

Here are the p25 experiments.

Odiv-210: piControl with Arctic bug

Only use years 1-100, transitioning to Odiv-230 for years 101-360.

Odiv-230: piControl with new code and Arctic bug fix

Started from 01JAN101 of Odiv-210 and used corrected Arctic and updates to the code to accept various minor bug fixes. This experiment ran until year 360.

Odiv-306: piControl extension from Odiv-230

Started from 01JAN361 of Odiv-230. Ran until year 1050.

Odiv-231: historical starting from Odiv-210

Historical started from 01JAN101 from Odiv-210 with corrected Arctic and updates to the code to accept various bug fixes. The initial time stamp is redefined as 01JAN1850, with this simulation running until 31DEC2014. It is directly comparable to its piControl partner, Odiv-230.

Odiv-232: SSP585 starting from Odiv-231

Started from 01Jan2015 from Odiv-231 using SSP585 forcing. Ran to 2100. It is directly comparable to its piControl partner, Odiv-230. Note that to produce 10-year postprocessing time series, we did a symlink of years 2010-2014 from Odiv-231 into Odiv-232.

19.3 CM4X-p125

Here are the p125 experiments.

Odiv-209: piControl with Arctic bug

This experiment ran beautifully for 350 years. But it used the Arctic bipolar bug. Odiv-313 is a rerun of years 101-350 with the bug fix (just like Odiv-230 for CM4X-p25).

Odiv-313: piControl with new code and Arctic bug fix: ran 250 years and is ongoing

Start from 01JAN101 of Odiv-209 and use corrected Arctic and updates to the code to accept the bug fixes. Run has completed to year 350 and now on windfall.This run will be analogous to the CM4X-p25 rerun in Odiv-210+Odiv-230.

Odiv-255: historical with new code and Arctic bug fix

Started from 01JAN101 of Odiv-209, with time stamp relabled to 01JAN1850 and to be run to 31DEC2014. This experiment is identical to Odiv-233 but Odiv-255 is run on the C5 computer. Odiv-233 was running on C4 and that machine started to degrade in reliability May/June 2023 so we halted Odiv-233 around year 1940 and moved to C5 with Odiv-255.

Odiv-293: SSP585 from year 2015 of Odiv-255

Start from 01Jan2015 from Odiv-255 using SSP585 forcing. Ran to 2100.

20 Further details on the CM4.0 and CM4X simulations

Here is a journal of the simulations according to their Dora numbers at GFDL, as well as their archive paths.

20.1 CM4.0

Odiv-001: piControl

The piControl for CM4.0 has been run for 650 years.

/archive/oar.gfdl.cmip6/CM4/warsaw_201710_om4_v1.0.1/CM4_piControl_C

Odiv-002: historical

The historical for CM4.0 runs from 1850 to 2014 and is at

/archive/oar.gfdl.cmip6/CM4/warsaw_201710_om4_v1.0.1/CM4_historical

SSP585

The SSP585 for CM4.0 is available at

/archive/oar.gfdl.cmip6/CM4/warsaw_201803_om4_v1.0.1 /CM4_Scenario_ssp585

20.2 CM4X-p25

Here are the main p25 experiments.

20.2.1 Odiv-210: piControl with Arctic bug

/archive/Raphael.Dussin/FMS2019.01.03_devgfdl_20210706/CM4_piControl_c192_OM4p25_v7/

This experiment ran beautifully for the PiControl for 250 years. Then, it crashed in year 293 over Libya. John Krasting recalled similar events in ESM4 development where the land model crashes with vanishing snow layers. The layers became very small and the radiative fluxes and surface temperatures go wild. It is unlikely there is snow in at that grid point in the Libyan desert, so something is amiss in the code. There was never a fix found. Rather, in ESM4 flipped the `make_exchange_reproduce` namelist option for that year to initiate some bit changes to enable the model to move through the crash.

We did the same namelist trick for Odiv-210 for year 293, thus enabling the model to run through the crash. For year 294 the flag was returned to its original setting. So here is a summary of the settings:

`make_exchange_reproduce = .true.`	for all years except 293
`make_exchange_reproduce = .false.`	for year 293

Note that there is no significant computational hit using `make_exchange_reproduce = .true.`, unlike in the CMIP3 days.

Given the Arctic bug described in Section 17, we only make use of years 0-100 of Odiv-210.

20.2.2 Odiv-226: piControl with Arctic bug fix

/archive/Raphael.Dussin/FMS2019.01.03_devgfdl_20210706/CM4_piControl_c192_OM4p25_v7_npolefix

This experiment started from year 250 of Odiv-210 and ran for 100 years to year 350. No significant change in the climate was detected, even in the Arctic. On 08Dec2022, we decided to take the Arctic bug fix moving forward, yet we will rerun the PiControl for both p25 and p125 starting from year 100 of each so that PiControl and historical/scenarios have identical code settings.

20.2.3 Odiv-227: piControl with Arctic bug fix and new MOM6 code

/archive/Raphael.Dussin/FMS2019.01.03_devgfdl_20210706/CM4_piControl_c192_OM4p25_v7_allfixes

Move to new MOM6 code. The following parameter settings were needed to reproduce Odiv-226:

- `#override INTERNAL_WAVE_SPEED_BETTER_EST = False`

- `#override EPBL_MLD_BISECTION = True`

This run verified that no major changes arising from the switch to new MOM6 code.

20.2.4 Odiv-230: piControl with new code and Arctic bug fix

/archive/Raphael.Dussin/FMS2019.01.03_devgfdl_20221223/CM4_piControl_c192_OM4p25_v8/

Started from 01JAN101 of Odiv-210 and used corrected Arctic and updates to the code to accept the bug fixes. This ran until year 360. This run is considered a success.

20.2.5 Odiv-306: piControl extension from Odiv-230

Started from 01JAN361 of Odiv-230. Ran to year 1050.

/archive/Raphael.Dussin/FMS2019.01.03_devgfdl_20221223/CM4_piControl_c192_OM4p25_v8/

20.2.6 Odiv-231: historical starting from Odiv-210

/archive/Raphael.Dussin/FMS2019.01.03_devgfdl_20221223/CM4_historical_c192_OM4p25

Historical started from 01JAN101 from Odiv-210 with corrected Arctic and updates to the code to accept bug fixes. The initial time stamp is redefined as 01JAN1850, with this simulation running until 31DEC2014. It is directly comparable to its piControl partner, Odiv-230.

20.2.7 Odiv-232: SSP5-8.5 starting from Odiv-231

/archive/Raphael.Dussin/FMS2019.01.03_devgfdl_20221223/CM4_ssp585_c192_OM4p25

Started from 01Jan2015 from Odiv-231 using SSP5-8.5 forcing. Ran to 2100. It is directly comparable to its piControl partner, Odiv-230. Note that to produce 10-year postprocessing time series, we did a symlink of years 2010-2014 from Odiv-231 into Odiv-232.

20.2.8 Odiv-343: instantaneous return to piControl from Odiv-231

/archive/Raphael.Dussin/FMS2019.01.03_devgfdl_20230608/CM4_piControl_c192_OM4p25_r2015

Started from 01Jan2015 of Odiv-231 with radiative forcing instantaneously returned to 1850 values seen in the piControl Odiv-230+Odiv-306.

20.3 CM4X-p125

Here are the main p125 experiments.

20.3.1 Odiv-209: piControl with Arctic bug

/archive/Raphael.Dussin/FMS2019.01.03_devgfdl_20210706/CM4_piControl_c192_OM4p125_v7

This experiment ran beautifully for 350 years. But it used the Arctic bipolar bug documented in Section 17.

20.3.2 Odiv-313: piControl with new code and Arctic bug fix

Start from 01JAN101 of Odiv-209 and use corrected Arctic and updates to the code to accept the bug fixes. Run as long as possible (at year 455 at 16 Oct 2024). This experiment is analogous to the CM4X-p25 experiment Odiv-230. Stopped around 16 Oct 2024 since machine architecture changed so will change answers.

/archive/Raphael.Dussin/FMS2019.01.03_devgfdl_20230608/CM4_piControl_c192_OM4p125_v8

20.3.3 Odiv-437: piControl with new code and Arctic bug fix on new architecture

Start from 01JAN451 of Odiv-313 with same code yet new machine architecture so that answers do not reproduce. Will continue running on windfall, with hopes to get to year 500 before paper published.

/archive/Raphael.Dussin/FMS2019.01.03_devgfdl_20241030/CM4_piControl_c192_OM4p125_v8followup

20.3.4 Odiv-233: historical with new code and Arctic bug fix on C4

/archive/Raphael.Dussin/FMS2019.01.03_devgfdl_20221223/CM4_historical_c192_OM4p125

Started from 01JAN101 of Odiv-209, with time stamp relabled to 01JAN1850 and to be run to 31DEC2014. Halted since C4 degraded. Picked up in Odiv-255.

20.3.5 Odiv-255: historical with new code and Arctic bug fix and run on C5

/archive/Raphael.Dussin/FMS2019.01.03_devgfdl_20230608/CM4_historical_c192_OM4p125/

Started from 01JAN101 of Odiv-209, with time stamp relabled to 01JAN1850 and to be run to 31DEC2014. This run is identical to Odiv-233 but Odiv-255 is run on the C5 computer. Odiv-233 was running on C4 and that machine started to degrade in reliability May/June 2023 so we halted Odiv-233 around year 1940 and moved to C5 with Odiv-255.

20.3.6 Odiv-293: SSP5-8.5 from Odiv-233

Start from 01Jan2015 from Odiv-233 using SSP5-8.5 forcing. Run to 2100.

/archive/Raphael.Dussin/FMS2019.01.03_devgfdl_20230608/CM4_ssp585_c192_OM4p125/

21 Open Research

We here document the datasets for building the CM4X models and in their evaluation; the software comprising the model; the software used for creating the figures; and the simulation datasets used to create the figures.

21.1 Datasets for building the model

Bottom topography

The bottom topography for the CM4X-p125 ocean is based on *GEBCO Compilation Group* (2021), and we downloaded this data from

```
https://www.gebco.net/data_and_products/gridded_bathymetry_data/
```

For the region south of 62°S, we transitioned to the BedMachine product from *Morlighem et al.* (2017), downloaded from

```
https://nsidc.org/data/nsidc-0756/versions/2
```

We placed the resulting bottom topography netCDF file onto the Zenodo link detailed in Section **??**.

Datasets for the tide induced mixing parameterization

For the tide mixing parameterization we use the TPX09 version of the Oregon State University barotropic shallow water tide model that uses methods from *Egbert and Erofeeva* (2002), with this dataset available from

```
https://www.tpxo.net/global/tpxo9-atlas
```

This tide model has a 1/30° grid spacing and we use the following eight harmonics: M2, S2, N2, K2, K1, O1, P1, Q1. The following repositories host the code to perform the interpolation of the tide amplitude onto the p25 and p125 grids:

```
https://github.com/raphaeldussin/OM4p25_tideamp
https://github.com/raphaeldussin/OM4p125_tideamp
```

21.2 Products used to evaluate CM4X

Here we detail those datasets and products used to evaluate the CM4X simulations.

Mixed layer depth

We used raw Argo data *Argo* (2023) for creating the mixed layer depths, with this data obtained from

```
dx.doi.org/10.17882/42182
```

where the snapshot from July 2023 was used for our analysis.

Sea level

In evaluating the sea level patterns, we made use of the GLORYS12 reanalysis product detailed in *Lellouche et al.* (2021) that is produced by the European Union Copernicus Marine Service Information. We accessed this product from *Lellouche et al.* (2021) using the web command

```
wget -m -no-parent
ftp://username:password@my.cmems-du.eu/Core/GLOBAL_MULTIYEAR_PHY_001_030/
```

Sea surface temperature patterns

To evaluate the sea surface temperature patterns, we made use of the NOAA OIv2 optimal interpolation product from *Huang et al.* (2020) and downloaded from

```
https://www.ncei.noaa.gov/products/optimum-interpolation-sst
```

Area mean sea surface temperature time series

For the sea surface temperature time series, we made use of the NOAA Extended Reconstructed SST V5 *Huang et al.* (2017), which was downloaded from

```
https://psl.noaa.gov/data/gridded/data.noaa.ersst.v5.html
```

Temperature and salinity initial conditions

We initialized the model using the potential temperature computed from the *in situ* temperature in *Locarnini et al.* (2018), and we used practical salinity from *Zweng et al.* (2018).

To evaluate upwelling

To evaluate eastern boundary upwelling, we made use of the SCOW windstress from *Risien and Chelton* (2008) and available for download from

```
https://chapman.ceoas.oregonstate.edu/scow/wind_stress_curl.html
```

We also used the sea surface temperature data from *Huang et al.* (2020).

References

Adcroft, A., Representation of topography by porous barriers and objective interpolation of topographic data, *Ocean Modelling*, *67*, 13–27, doi:10.1016/j.ocemod.2013.03.002, 2013.

Adcroft, A., W. Anderson, C. Blanton, M. Bushuk, C. O. Dufour, J. P. Dunne, S. M. Griffies, R. W. Hallberg, M. J. Harrison, I. Held, M. Jansen, J. John, J. P. Krasting, A. Langenhorst, S. Legg, Z. Liang, C. McHugh, B. G. Reichl, A. Radhakrishnan, T. Rosati, B. Samuels, A. Shao, R. J. Stouffer, M. Winton, A. T. Wittenberg, B. Xiang, N. Zadeh, and R. Zhang, The GFDL global ocean and sea ice model OM4.0: Model description and simulation features, *Journal of Advances in Modeling the Earth System*, *JAMES*, doi:10.1029/2019MS001726, 2019.

Argo, Argo float data and metadata from Global Data Assembly Centre (Argo GDAC), doi:10.17882/42182, 2023.

Bleck, R., An oceanic general circulation model framed in hybrid isopycnic-Cartesian coordinates, *Ocean Modelling*, *4*, 55–88, doi:10.1016/S1463-5003(01)00012-9, 2002.

Boccaletti, G., R. Ferrari, and B. Fox-Kemper, Mixed layer instabilities and restratification, *Journal of Physical Oceanography*, *35*, 1263–1278, doi:10.1175/JPO3101.1, 2007.

Briegleb, B. P., and B. Light, A delta-Eddington multiple scattering parameterization for solar radiation in the sea ice component of the Community Climate System Model, *Technical Report TN-4721+STR*, National Center for Atmospheric Research, Boulder, USA, 2007.

Delworth, T. L., W. F. Cooke, A. Adcroft, M. Bushuk, J.-H. Chen, K. A. Dunne, P. Ginoux, R. Gudgel, R. W. Hallberg, L. Harris, et al., SPEAR: The next generation GFDL modeling system for seasonal to multidecadal prediction and projection, *Journal of Advances in Modeling Earth Systems*, *12*(3), e2019MS001,895, 2020.

Dunne, J. P., L. W. Horowitz, A. Adcroft, P. Ginoux, I. M. Held, J. G. John, J. P. Krasting, S. Malyshev, V. Naik, F. Paulot, E. Shevliakova, C. A. Stock, N. Zadeh, C. Blanton, V. Balaji, J. Durachta, K. A. Dunne, C. Dupuis, P. P. G. Gauthier, S. M. Griffies, H. Guo, R. W. Hallberg, M. Harrison, J. He, W. Hurlin, R. Menzel, P. C. D. Milly, C. McHugh, S. Nikonov, D. J. Paynter, J. Ploshay, A. Radhakrishnan, K. Rand, T. Robinson, D. M. Schwarzkopf, C. J. Seman, S. Underwood, H. Vahlenkamp, M. Winton, B. Wyman, Y. Zeng, and M. Zhao, The GFDL Earth system model version 4.1 (GFDL-ESM4.1): Model description and simulation characteristics, *Journal of Advances in Modeling Earth Systems*, *12*, doi:10.1029/2019MS002015, 2020.

Egbert, G. D., and S. Y. Erofeeva, Efficient inverse modeling of barotropic ocean tides, *Journal of Atmospheric and Oceanic Technology*, *19*, 183–204, doi:10.1175/1520-0426(2002)019⟨0183:EIMOBO⟩2.0.CO;2, 2002.

Fox-Kemper, B., R. Ferrari, and R. Hallberg, Parameterization of mixed layer eddies. I: Theory and diagnosis, *Journal of Physical Oceanography*, *38*, 1145–1165, doi:10.1175/2007JPO3792.1, 2008.

Fox-Kemper, B., G. Danabasoglu, R. Ferrari, S. M. Griffies, R. W. Hallberg, M. M. Holland, S. Peacock, and B. Samuels, Parameterization of mixed layer eddies. III: Global implementation and impact on ocean climate simulations, *Ocean Modelling*, *39*, 61–78, doi:10.1016/j.ocemod.2010.09.002, 2011.

GEBCO Compilation Group, GEBCO 2021 Grid, doi:10.5285/c6612cbe-50b3-0cff-e053-6c86abc09f8f, 2021.

Griffies, S. M., and A.-M. Treguier, Ocean models and ocean modeling, in *Ocean Circulation and Climate, 2nd Edition: A 21st Century Perspective*, *International Geophysics Series*, vol. 103, edited by G. Siedler, S. M. Griffies, J. Gould, and J. Church, pp. 521–552, Academic Press, doi:10.1016/B978-0-12-391851-2.00020-9, 2013.

Griffies, S. M., M. Winton, W. G. Anderson, R. Benson, T. L. Delworth, C. Dufour, J. P. Dunne, P. Goddard, A. K. Morrison, A. Rosati, A. T. Wittenberg, J. Yin, and R. Zhang, Impacts on ocean heat from transient mesoscale eddies in a hierarchy of climate models, *Journal of Climate*, *28*, 952–977, doi:10.1175/JCLI-D-14-00353.1, 2015.

Griffies, S. M., A. Adcroft, and R. W. Hallberg, A primer on the vertical Lagrangian-remap method in ocean models based on finite volume generalized vertical coordinates, *Journal of Advances in Modeling Earth Systems*, *12*, doi:10.1029/2019MS001954, 2020.

Griffies, S. M., A. Adcroft, R. L. Beadling, M. Bushuk, C.-Y. Chang, H. F. Drake, R. Dussin, R. W. Hallberg, W. J. Hurlin, H. Khatri, J. P. Krasting, M. Lobo, G. A. MacGilchrist, B. G. Reichl, A. Sane, O. Sergienko, M. Sonnewald, J. M. Steinberg, J.-E. Tesdel, M. Thomas, K. E. Turner, M. Ward, M. Winton, N. Zadeh, R. Zhang, W. Zhang, and M. Zhao, The GFDL-CM4X climate model hierarchy, Part I: model description and thermal properties, *Journal of Advances in Modeling Earth Systems (JAMES)*, *17*, doi:10.1029/2024MS004861, 2025a.

Griffies, S. M., A. Adcroft, R. L. Beadling, M. Bushuk, C.-Y. Chang, H. F. Drake, R. Dussin, R. W. Hallberg, W. J. Hurlin, H. Khatri, J. P. Krasting, M. Lobo, G. A. MacGilchrist, B. G. Reichl, A. Sane, O. Sergienko, M. Sonnewald, J. M. Steinberg, J.-E. Tesdel, M. Thomas, K. E. Turner, M. Ward, M. Winton, N. Zadeh, R. Zhang, W. Zhang, and M. Zhao, The GFDL-CM4X climate model hierarchy, Part II: case studies, *Journal of Advances in Modeling Earth Systems (JAMES)*, *17*, doi:10.1029/2024MS004862, 2025b.

Hallberg, R. W., Using a resolution function to regulate parameterizations of oceanic mesoscale eddy effects, *Ocean Modelling*, *72*, 92–103, doi:10.1016/j.ocemod.2013.08.007, 2013.

Held, I. M., Gap between simulation and understanding in climate modeling, *Bulletin of the American Meteorological Society*, *86*, 1609–1614, doi:10.1175/BAMS-86-11-1609, 2005.

Held, I. M., H. Guo, A. Adcroft, J. P. Dunne, L. W. Horowitz, J. Krasting, E. Shevliakova, M. Winton, M. Zhao, M. Bushuk, A. T. Wittenberg, B. Wyman, B. Xiang, R. Zhang, W. Anderson, V. Balaji, L. Donner, K. Dunne, J. Durachta, P. P. G. Gauthier, P. Ginoux, J.-C. Golaz, S. M. Griffies, R. Hallberg, L. Harris, M. Harrison, W. Hurlin, J. John,

P. Lin, S.-J. Lin, S. Malyshev, R. Menzel, P. C. D. Milly, Y. Ming, V. Naik, D. Paynter, F. Paulot, V. Rammaswamy, B. Reichl, T. Robinson, A. Rosati, C. Seman, L. G. Silvers, S. Underwood, and N. Zadeh, Structure and performance of GFDL's CM4.0 climate model, *Journal of Advances in Modeling the Earth System*, *11*, 3691–3726, doi:10.1029/2019MS001829, 2019.

Henyey, F. S., J. Wright, and S. M. Flatte, Energy and action flow through the internal wave field: an eikonal approach, *Journal of Geophysical Research*, *91*, 8487–8496, doi:10.1029/JC091iC07p08487, 1986.

Hofstadter, D. R., *Gödel, Escher, Bach: An Eternal Golden Braid*, Basic Books, 777 pages, 1979.

Hu, C., Z. Lee, and B. Franz, Chlorophyll-a algorithms for oligotrophic oceans: a novel approach based on three-band reflectance difference map of solid earth surface heat flow, *Journal of Geophysical Research*, *117, C01011*, doi:10.1029/2011JC007395, 2012.

Huang, B., P. W. Thorne, V. F. Banzon, T. Boyer, G. Chepurin, J. H. Lawrimore, M. J. Menne, T. M. Smith, R. S. Vose, , and H.-M. Zhang, NOAA Extended Reconstructed Sea Surface Temperature (ERSST), Version 5, *dataset*, NOAA National Centers for Environmental Information, U.S. Department of Commerce, Washington, D.C., doi:0.7289/V5T72FNM, 2017.

Huang, B., C. Liu, V. Banzon, E. Freeman, G. Graham, B. Hankins, T. Smith, and H.-M. Zhang, Improvements of the daily optimum interpolation sea surface temperature (DOISST) Version 2.1, *Journal of Climate*, *34*, 2923–2939, doi:10.1175/JCLI-D-20-0166.1, 2020.

Huw Davies, J., Global map of solid Earth surface heat flow, *Geochemistry, Geophysics, Geosystems*, *14*, 4608–4622, doi:10.1002/ggge.20271, 2013.

Huynh, H. T., Schemes and constraints for advection, in *Proceedings of the Fifteenth International Conference on Numerical Methods in Fluid Dynamics, Monterey, Ca, USA, 24-28 June 1996*, doi:doi:10.1007/BFb0107151, 1996.

Jackson, L., R. W. Hallberg, and S. Legg, A parameterization of shear-driven turbulence for ocean climate models, *Journal of Physical Oceanography*, *38*, 1033–1053, doi:10.1175/2007JPO3779.1, 2008.

Jeevanjee, N., P. Hassanzadeh, S. Hill, and A. Sheshadri, A perspective on climate model hierarchies, *Journal of Advances in Modeling Earth Systems*, *9*, 1760–1771, doi:10.1002/2017MS001038, 2017.

Kiss, A. E., A. M. Hogg, N. Hannah, F. B. Dias, G. Brassington, M. A. Chamberlain, C. Chapman, P. Dobrohotoff, C. Domingues, E. R. Duran, M. H. England, R. Fiedler, S. M. Griffies, A. Heerdegen, P. Heil, R. H. Holmes, A. Klocker, S. J. Marsland, A. K. Morrison, J. Munroe, M. Nikurashin, P. Oke, G. S. Pilo, O. Richet, A. Savita, J. P. Spence, K. D. Stewart, M. L. Ward, F. Wu, and X. Zhang, ACCESS-OM2: A global ocean-sea ice model at three resolutions, *Geoscientific Model Development*, doi:10.5194/gmd-13-401-2020, 2020.

Legg, S., R. W. Hallberg, and J. B. Girton, Comparison of entrainment in overflows simulated by z-coordinate, isopycnal and non-hydrostatic models, *Ocean Modelling*, *11*(1), 69–97, doi:10.1016/j.ocemod.2004.11.006, 2006.

Lellouche, J.-M., E. Greiner, R. Bourdallé-Badie, G. Garric, A. Melet, M. Drévillon, C. Bricaud, M. Hamon, O. Le Galloudec, C. Regnier, T. Candela, C.-E. Testut, C.-E. Testut, F. Gasparin, G. Ruggiero, M. Benkiran, Y. Drillet, and P.-Y. Le Traon, The Copernicus global 1/12° oceanic and sea ice GLORYS12 reanalysis, *Frontiers in Earth Science*, *9*, doi:10.3389/feart.2021.698876, 2021.

Locarnini, R. A., A. V. Mishonov, O. K. Baranova, T. P. Boyer, M. M. Zweng, H. E. Garcia, J. R. Reagan, D. Seidov, K. Weathers, C. R. Paver, and I. Smolyar, World Ocean Atlas 2018, Volume 1: Temperature, *dataset*, NOAA/NESDIS, U.S. Department of Commerce, Washington, D.C., 2018.

Manizza, M., C. Le Quere, A. J. Watson, and E. T. Buitenhuis, Bio-optical feedbacks among phytoplankton, upper ocean physics and sea-ice in a global model, *Geophysical Research Letters*, *32*(5), doi:10.1029/2004GL020778, 2005.

Marques, G. M., N. Loose, E. Yankovsky, J. M. Steinberg, C.-Y. Chang, N. Bhamidipati, A. Adcroft, B. Fox-Kemper, S. M. Griffies, R. Hallberg, M. F. Jansen, H. Khatri, and L. Zanna, Neverworld2: An idealized model hierarchy to investigate ocean mesoscale eddies across resolutions, *Geoscientific Model Development*, doi:10.5194/gmd-15-6567-2022, 2022.

McDougall, T. J., P. M. Barker, R. M. Holmes, R. Pawlowicz, S. M. Griffies, and P. J. Durack, The interpretation of temperature and salinity variables in numerical ocean model output and the calculation of heat fluxes and heat content, *Geoscientific Model Development*, *14*, 6445–6466, doi:10.5194/gmd-14-6445-2021, 2021.

Melet, A., R. W. Hallberg, S. Legg, and K. Polzin, Sensitivity of the Pacific Ocean state to the vertical distribution of internal-tide driven mixing, *Journal of Physical Oceanography*, *43*, 602–615, doi:10.1175/JPO-D-12-055.1, 2013.

Morlighem, M., C. N. Williams, E. Rignot, L. An, J. E. Arndt, J. L. Bamber, G. Catania, N. Chauché, J. A. Dowdeswell, B. Dorschel, I. Fenty, K. Hogan, I. Howat, A. Hubbard, M. Jakobsson, T. M. Jordan, K. K. Kjeldsen, R. Millan, L. Mayer, J. Mouginot, B. P. Y. Noël, C. O'Cofaigh, S. Palmer, S. Rysgaard, H. Seroussi, M. J. Siegert, P. Slabon, F. Straneo, M. R. van den Broeke, W. Weinrebe, M. Wood, , and K. B. Zinglersen, Bedmachine v3: Complete bed topography and ocean bathymetry mapping of greenland from multibeam echo sounding combined with mass conservation, *Geophysical Research Letters*, *44*, 11,051–11,061, doi:10.1002/2017GL074954, 2017.

Reichl, B. G., and R. W. Hallberg, A simplified energetics based planetary boundary layer (ePBL) approach for ocean climate simulations, *Ocean Modelling*, *132*, 112–129, doi:10.1016/j.ocemod.2018.10.004, 2018.

Reichl, B. G., and Q. Li, A parameterization with a constrained potential energy conversion rate of vertical mixing due to Langmuir turbulence, *Journal of Physical Oceanography*, *49*, 2935–2959, doi:10.1175/JPO-D-18-0258.1, 2019.

Risien, C. M., and D. B. Chelton, A global climatology of surface wind and wind stress fields from eight years of QuikSCAT scatterometer data, *Journal of Physical Oceanography*, *38*(11), 2379 – 2413, doi:https://doi.org/10.1175/2008JPO3881.1, 2008.

Sadourny, R., The Dynamics of Finite-Difference Models of the Shallow-Water Equations, *Journal of the Atmospheric Sciences*, *32*(4), 680–689, doi:10.1175/1520-0469(1975)032⟨0680:TDOFDM⟩2.0.CO;2, 1975.

Simmons, H. L., S. R. Jayne, L. C. St.Laurent, and A. J. Weaver, Tidally driven mixing in a numerical model of the ocean general circulation, *Ocean Modelling*, *6*, 245–263, doi:10.1016/S1463-5003(03)00011-8, 2004.

St. Laurent, L. C., H. L. Simmons, and S. R. Jayne, Estimating tidally driven energy in the deep ocean, *Geophysical Research Letters*, *29*, 2106–2110, doi:10.1029/2002GL015, 2002.

Tozer, B., D. T. Sandwell, W. H. F. Smith, C. Olson, J. R. Beale, and P. Wessel, Global bathymetry and topography at 15 arc sec: Srtm15+, *Earth and Space Science*, *6*, 1847–1864, doi:10.1029/2019EA000658, 2019.

White, L., and A. Adcroft, A high-order finite volume remapping scheme for nonuniform grids: The piecewise quartic method (PQM), *Journal of Computational Physics*, *227*, 7394–7422, doi:10.1016/j.jcp.2008.04.026, 2008.

White, L., A. Adcroft, and R. W. Hallberg, High-order regridding-remapping schemes for continuous isopycnal and generalized coordinates in ocean models, *Journal of Computational Physics*, *228*, doi:10.1016/j.jcp.2009.08.016, 2009.

Wright, D. G., An equation of state for use in ocean models: Eckart's formula revisited, *Journal of Atmospheric and Oceanic Technology*, *14*, 735–740, doi:10.1175/1520-0426(1997)014⟨0735:AEOSFU⟩2.0.CO;2, 1997.

Zhang, L., T. L. Delworth, W. Cooke, H. Goosse, M. Bushuk, Y. Morioka, and X. Yang, The dependence of internal multidecadal variability in the Southern Ocean on the ocean background mean state, *Journal of Climate*, *34*(3), 1061–1080, doi:0.1175/JCLI-D-20-0049.1, 2021.

Zhao, M., Simulations of atmospheric rivers, their variability, and response to global warming using GFDL's new high-resolution general circulation model, *Journal of Climate*, *33*, 10,287–10,303, doi:10.1175/JCLI-D-20-0241.1, 2020.

Zweng, M. M., J. R. Reagan, D. Seidov, T. P. Boyer, R. A. Locarnini, H. E. Garcia, A. V. Mishonov, O. K. Baranova, K. Weathers, C. R. Paver, and I. Smolyar, World Ocean Atlas 2018, Volume 2: Salinity, *dataset*, NOAA/NESDIS, U.S. Department of Commerce, Washington, D.C., 2018.